

1 Reliability of lumped hydrological modeling in a semi-arid 2 mountainous catchment facing water-use changes

3
4 P. HUBLART^{1,7}, D. RUELLAND², I. GARCÍA DE CORTÁZAR-ATAURI³, S.
5 GASCOIN⁴, S. LHERMITTE⁵ and A. IBACACHE⁶

6 [1] {UM2, UMR HydroSciences Montpellier, Montpellier, France}

7 [2] {CNRS, UMR HydroSciences Montpellier, Montpellier, France}

8 [3] {INRA, US 1116 AGROCLIM, Avignon, France}

9 [4] {CNRS, CESBIO, UMR 5126, Toulouse, France}

10 [5] {KU LEUVEN, Division of Geography, Leuven, Belgium}

11 [6] {INIA, Colina San Joaquín s/n, La Serena, Chile}

12 [7] {CEAZA, Raúl Bitrán s/n, La Serena, Chile}

13 Correspondence to: P. Hublart (p.hublart@gmail.com)

14 15 16 **Abstract**

17
18 This paper explores the reliability of a hydrological modeling framework in a mesoscale
19 (1515 km²) catchment of the dry Andes (30°S) where irrigation water-use and snow
20 sublimation represent a significant part of the annual water balance. To this end, a 20-year
21 simulation period encompassing a wide range of climate and water-use conditions was
22 selected to evaluate three types of integrated Models referred to as A, B and C. These Models
23 share the same runoff generation and routing module but differ in their approach to snowmelt
24 modeling and irrigation water-use. Model A relies on a simple degree-day approach to
25 estimate snowmelt rates and assumes that irrigation impacts can be neglected at the catchment
26 scale. Model B ignores irrigation impacts just as Model A but uses an enhanced degree-day
27 approach to account for the effects of net radiation and sublimation on melt rates. Model C
28 relies on the same snowmelt routine as Model B but incorporates irrigation impacts on natural
29 streamflow using a conceptual irrigation module. Overall, the reliability of probabilistic
30 streamflow predictions was greatly improved with Model C, resulting in narrow uncertainty
31 bands and reduced structural errors, notably during dry years. This model-based analysis also

32 stressed the importance of considering sublimation in empirical snowmelt models used in the
33 subtropics, and provided evidence that water abstractions from the unregulated river is
34 impacting on the hydrological response of the system. This work also highlighted areas
35 requiring additional research, including the need for a better conceptualization of runoff
36 generation processes in the dry Andes.

37

38

39 **1. Introduction**

40

41 Mountains act as natural water towers in many semi-arid regions. Glaciers and seasonal
42 snowpack in the uplands serve as reservoirs, accumulating water during the winter and
43 sustaining streams and aquifers during the spring and summer. This reduces streamflow
44 variability in the lowlands and provides local communities with the opportunity to develop
45 agricultural systems based on regular water supplies. Irrigation often represents a large part of
46 crop water-use in these areas due to the dry conditions that prevail during the growing season
47 [Siebert and Döll, 2010].

48 This makes such systems highly vulnerable to projected changes in climate conditions, for
49 at least two reasons. First, warmer temperatures will reduce the fraction of precipitation
50 falling as snow and tend to accelerate snowmelt, leading to earlier and reduced spring peak
51 flows and increased winter flows [Adam et al., 2009; Sproles et al., 2013]. Reduced summer
52 and fall flows could in turn significantly impact water availability for irrigation purposes.
53 Second, higher temperatures in the valleys will affect the timing of phenological events
54 [Cleland et al., 2007], which drive the seasonal pattern of crop water needs. Some perennial
55 crops like grapevines are already showing a tendency toward earlier budburst events and
56 shortened growth intervals in many regions of the world [Jones et al., 2005; Duchêne et al.,
57 2010a]. Vineyards located in semi-arid mountainous areas are particularly exposed, owing to
58 high diurnal temperature variations and overall sub-optimal growing temperatures [Caffarra
59 and Eccel, 2011]. It has also been noted that elevated temperatures may adversely affect the
60 ability to meet chilling requirements during the crop dormancy [Webb et al., 2007].

61 Thus, the future of agricultural systems in snow-dominated, semi-arid catchments relies on
62 our ability to anticipate the complex relationships between climate conditions, snowmelt
63 timing, water availability and crop water-use.

64

65 **1.1. Advantages and limitations of current conceptual precipitation-runoff** 66 **models**

67
68 To understand and forecast the response of hydrological systems, hydrologists often rely on
69 numerical catchment models known as ‘conceptual precipitation-runoff models’. Precipitation
70 inputs are processed into runoff through a number of inter-connected water stores
71 representing different aspects of the system's behavior (e.g. slow vs. fast responses, surface-
72 water vs. groundwater compartments). In general, relatively simple structures are used, in
73 which typically less than 10 parameters require calibration against physically observable
74 responses (e.g. streamflow data) [Wagener et al., 2001]. Such models also have low data and
75 computer requirements, making them especially attractive in data-scarce areas such as remote
76 mountainous catchments. As a result, they are being increasingly used to evaluate the
77 potential impacts of land-use and/or climate changes on the capacity to meet agricultural
78 water demands [e.g. Merritt et al., 2004; Collet et al., 2015; Fabre et al., 2015a].

79 The conclusions drawn from these models, however, are naturally bounded by a range of
80 uncertainty arising from multiple sources of error and approximations. This includes the
81 impacts of input data errors, numerical approximations, structural inadequacies and model
82 non-uniqueness. Parameter instability under changing climate and/or anthropogenic
83 conditions represents an additional source of uncertainty that may be difficult to distinguish
84 from parameter equifinality in the absence of uncertainty analysis [Seibert and McDonnell,
85 2010; Brigode et al., 2013]. Such limitations remain largely overlooked in many impact
86 studies. Instead, it is often assumed that the uncertainty associated with climate and/or water-
87 use scenarios greatly outweighs that arising from the modeling process itself. From a water
88 management perspective, however, the added value of precipitation-runoff models lies not
89 simply in their ability to provide accurate streamflow predictions but also in the systematic
90 examination of the uncertainty surrounding these predictions and the ultimate decision being
91 addressed [Ajami et al., 2008].

92 One of the most effective means of providing such information is through the use of
93 Bayesian inference methods. Notwithstanding important issues in how best to handle
94 epistemic uncertainties, and whether probability theory is the right tool to use [Beven et al.,
95 2011; Montanari, 2011], formal Bayesian approaches offer the opportunity to test the
96 reliability of model predictions through a series of posterior diagnostics. This, in turn,
97 provides a meaningful way to discuss the relative merits of competing model structures or
98 different versions of the same model. Very often, structural inadequacies can be partially

99 alleviated by comparing alternative representations of the processes at work. This paper
100 addresses two specific issues pertaining to the use of conceptual models in semi-arid
101 catchments where the effects of irrigation water-use and snow sublimation cannot be
102 dismissed *a priori*.

103

104 **1.2. Potential impacts of water abstraction and irrigation water-use**

105

106 The first issue deals with water abstraction for irrigation, which has many potential impacts
107 on hydrological processes, including changes in groundwater recharge [Scanlon et al., 2006]
108 and low-flow characteristics [Yang et al., 2010]. In arid and semi-arid catchments, these
109 impacts may be hard to quantify because a high degree of temporal and spatial variability in
110 climate conditions often mask anthropogenic trends [Kim et al., 2007]. During low-flow and
111 drought periods, however, a much greater proportion of natural flow may be abstracted,
112 leading to amplified impacts (in relative terms) on the flow regime. The poor performance of
113 most conceptual models during these critical periods is a well-recognized issue in the
114 hydrological research community and many studies have formulated different approaches
115 towards improving low-flow simulations [e.g. Smith et al., 2010; Staudinger et al., 2011;
116 Pushpalatha et al., 2011]. Yet, most of these studies have been concerned mainly with
117 undisturbed river systems. The impacts of river damming and regulation have also been
118 studied extensively, but there is a surprising dearth of work regarding the effects of water
119 abstraction from unregulated streams.

120 A common approach to remove such effects in model building and evaluation is to rely on
121 ‘naturalized’ streamflow data [e.g. Ashagrie et al., 2006]. This requires detailed information
122 on surface or ground water withdrawals and irrigation water-use, which is rarely available. In
123 practice, the sum of all water access entitlements is often taken as an upper bound for the
124 actual water consumption at the catchment scale, and added back to observed streamflow data
125 before calibrating a given model. Yet, farmers may not withdraw their full entitlement all year
126 long and a significant part of water withdrawals actually return to the river system within a
127 few days or weeks due to conveyance and field losses. In theory, ignoring these return flows
128 would lead to overestimating natural streamflow. But in reality, it can be very difficult to
129 disentangle the relative influence of epistemic errors in streamflow estimates (rating curve
130 errors, unknown return flows) and input data (precipitation, temperature, potential
131 evapotranspiration). Therefore, for a proper assessment of model reliability, streamflow
132 naturalization should be considered an integral part of the modeling process and explicitly

133 recognized as an additional source of imprecision in streamflow predictions [Hughes and
134 Mantel, 2010; Hublart et al., 2015a].

135

136 **1.3. Potential impacts of sublimation losses**

137

138 The second issue addressed by this paper concerns the means by which snowmelt inputs are
139 obtained in snow-dominated, semi-arid catchments. Many studies rely on empirical degree-
140 day approaches, in which air temperature is taken as a reasonable proxy for the energy
141 available for melt [Ohmura, 2001]. Melt rates are assumed to be linearly related to air
142 temperature by a constant of proportionality known as the ‘melt factor’, which can vary on a
143 seasonal basis [Hock, 2003]. Enhanced degree-day methods are sometimes implemented to
144 include the effects of additional variables such as solar radiation or wind speed. However, by
145 focusing exclusively on melt rates, such approaches can prove highly misleading where
146 sublimation losses represent a large part of ablation rates. This is generally the case in semi-
147 arid areas located around 30°S and 30°N.

148 Sublimation rates in the subtropics are expected to be high as a result of very low relative
149 humidity and intense solar radiation during most of the year. In the dry Andes, for instance,
150 Gascoin et al. [2013] found that sublimation losses represented more than 70% of the total
151 ablation simulated by a physically-based model in the instrumented site of Pascua-Lama
152 (1043 km², 2600–5630 m a.s.l.). Similar results were also obtained by experimental studies
153 conducted on small glaciers of the same region [MacDonell et al., 2013]. In the Northern
154 Hemisphere, Schulz and de Jong [2004] attributed up to 44% of annual snow ablation to
155 sublimation in a 140 km² catchment of the High Atlas range (2000–4000 m a.s.l.). It is
156 becoming increasingly recognized that failure to account for sublimation losses in commonly-
157 used temperature-index methods can impair model performance, distort parameter
158 identification and question the reliability of snowmelt estimates under higher temperatures
159 [e.g. Boudhar et al., 2009; Ayala et al., 2015].

160

161 **1.4. Objectives**

162

163 Ideally, the incorporation of new processes into a given model structure should be achieved
164 using the same level of mathematical abstraction and process representation as in the original
165 model. Blöschl and Montanari [2010] insisted that “a better understanding of the hydrological
166 processes should not necessarily translate into more complex models used in impact studies”.

167 Indeed, maintaining low-dimensional, holistic modeling approaches is essential to constrain
168 parameter uncertainty and help the modelers focus on understanding the main drivers of
169 hydrological change.

170 This paper investigates one possible way of integrating the effects of irrigation water-use
171 and snow sublimation into a parsimonious, catchment-scale modeling framework. Such
172 processes are typically not accounted for in currently available precipitation-runoff models.
173 Particular attention is paid to the representation of changes in irrigated areas and crop
174 varieties over time. The method is tested in a snowmelt-fed catchment of the Coquimbo
175 region (Chile) , which is currently facing one of the worst droughts in its recorded history
176 [Salinas et al., 2015]. In the same catchment, Hublart et al. (2015a) attempted to reduce
177 structural uncertainty in a non-probabilistic way by comparing 72 alternative models derived
178 from the same modular framework. However, the potential effects of irrigation and
179 sublimation were not included in this multiple-hypothesis framework, thereby limiting its
180 ability to cope with climate and anthropogenic changes. Hublart et al. (2015b) provided a first
181 attempt to incorporate these two processes in a precipitation-runoff model, but several
182 important aspects, such as the quantification of model uncertainty and the quality of snowmelt
183 simulations, remained outside the scope of their study. Compared to this previous paper, the
184 present study makes use of (1) extended calibration and validation periods to encompass a
185 wider range of climate and water-use conditions, (2) formal Bayesian theory to quantify
186 predictive uncertainty in a probabilistic way, and (3) remotely-sensed snow-cover data to
187 evaluate the internal consistency of the snow module.

188

189

190 **2. Study area and data**

191

192 **2.1. General setting**

193

194 **2.1.1. Physical landscape**

195

196 The Claro River catchment is a semi-arid, mountainous catchment located in North-Central
197 Chile (30°S). It drains an area of about 1 515 km² characterized by a series of granitic
198 mountain blocks interspersed with steep-sided valleys. Elevations range from 820 m a.s.l. at
199 the catchment outlet in Rivadavia to approximately 5500 m a.s.l. near the border with
200 Argentina (Fig. 1a). Above 3000 m a.s.l., repeated glaciations and the continuous action of

201 frost and thaw throughout the year have caused an intense shattering of the exposed rocks,
202 leaving a landscape of bare rock and screes almost devoid of soil. The valley-fill material
203 consists of mostly unconsolidated glaciofluvial and alluvial sediments mantled by generally
204 thin soils (< 1 m) of sandy to sandy-loam texture. Natural vegetation outside the valleys is
205 extremely sparse and composed mainly of subshrubs (e.g. *Adesmia echinus*) and cushion
206 plants (e.g. *Laretia acaulis*) with very low transpiration rates [Squeo et al., 1993; Kalthoff et
207 al., 2006]. In the lower part of the catchment, vineyards and orchards cover most of the valley
208 floors and lower hill slopes, where they benefit from a unique combination of clear skies, high
209 diurnal temperature variations and overall dry conditions during the growing season. The
210 Claro River originates from a number of small, snowmelt-fed tributaries flowing either
211 permanently or seasonally in the mountains.

212

213 **2.1.2. Climate**

214

215 Most of the annual precipitation falls as snow during typically 2 or 3 winter storms [Favier et
216 al., 2009], when the South Pacific High reaches its northernmost position (June–August).
217 Mean annual precipitation ranges from approximately 100 mm at the catchment outlet
218 (Rivadavia) to 670 mm in the High Cordillera [Bourgin et al., 2012]. The annual snow cover
219 duration estimated from MODIS snow-covered area (SCA) data (see Sect. 2.2.) ranges from
220 less than 20–40 days at low elevations (< 2000 m a.s.l.) to about 160–180 days at high
221 elevations (> 4000 m a.s.l.), where sublimation is expected to be the dominant cause of
222 ablation [Gascoïn et al., 2013; MacDonell et al., 2013]. In the dry Andes, net shortwave
223 radiation represents the dominant source of energy available for melt and sublimation
224 [Pelliciotti et al., 2008].

225 At the inter-annual timescale, the El Niño Southern Oscillation (ENSO) represents the
226 largest source of climate variability [Montecinos and Aceituno, 2003]. Anomalously wet (dry)
227 years in the region are generally associated with warm (cold) El Niño (La Niña) episodes and
228 a simultaneous weakening (strengthening) of the South Pacific High. It is worth noting,
229 however, that some very wet years in the catchment can also coincide with neutral to weak La
230 Niña conditions, as in 2000–2001, while several years of below-normal precipitation may not
231 exhibit clear La Niña characteristics [Verbist et al., 2010]. These anomalies may be due to
232 other modes of climate variability affecting the Pacific basin on longer timescales. The
233 Interdecadal Pacific Oscillation (IPO), in particular, has been shown to modulate ENSO's
234 influence according to cycles of 15 to 30 years [Schulz et al., 2011]. Figure 1c shows a

235 sustained decrease in mean annual streamflow since the mid-1990s, which could be associated
236 with a shift in the IPO phase around 1998.

237

238 **2.1.3. Agricultural activity**

239

240 Grape growing is by far the main agricultural activity in the catchment. All grapes are grown
241 to be exported as early-season table grapes or processed into a brandy-like national drink
242 known as *pisco*. Reliable water supplies are critical to satisfy crop water needs in the summer,
243 since precipitation events occur mostly at high elevations or outside the growing season.
244 Irrigation water is diverted at multiple locations along the river's course and conveyed to the
245 fields through a complex network of open, mostly unlined canals. The amount of water
246 diverted from the river depends on both historical water rights and current water availability.
247 Table varieties are mostly drip-irrigated while pisco varieties remain largely furrow-irrigated.

248 Irrigated areas in the Claro River catchment have increased by about 200% between 1985
249 and 2005 (Fig. 1b). This expansion has been limited by both water and agricultural land
250 availability, and irrigated areas currently represent less than 5% of the total catchment area. A
251 rough estimate of the effects of increased irrigated areas on mean annual streamflow can be
252 obtained by looking at the difference in discharge measured at Rivadavia (downstream from
253 cultivated areas) and that measured at Cochiguaz and Alcohuaz (upstream from cultivated
254 areas) (Fig. 1c). Note that transmission losses caused by infiltration through the riverbed may
255 also reduce streamflow at downstream points, especially during dry periods when the depth of
256 water tables is low.

257

258 **2.2. Materials**

259

260 **2.2.1. Hydro-climate data**

261

262 Precipitation and temperature data were interpolated from respectively 12 and 8 stations to a 5
263 × 5 km grid using an inverse distance squared weighting [Ruelland et al., 2014]. Orographic
264 effects on precipitation were considered using the approach described in Valéry et al. [2010a]
265 with a correction factor of $6.5 \cdot 10^{-4} \text{ m}^{-1}$ (determined by sensitivity analysis), resulting in a
266 gradient of around 0.4 m water equivalent per km. For temperature, a constant lapse rate of -
267 $6.0^\circ\text{C km}^{-1}$ was estimated from the observed data. Daily streamflow data were extracted from
268 the Chilean *Dirección General de Aguas*' database.

269 In addition, remotely-sensed data from the MODerate resolution Imaging
270 Spectroradiometer (MODIS) sensor were introduced to estimate the seasonal patterns of
271 fractional snow-covered areas (F_{SCA}) over a 12 year period (2000–2011). Daily snow cover
272 products retrieved from NASA’s Terra (MOD10A1) and Aqua (MYD10A1) satellites were
273 combined into a single, composite 500 m resolution product to reduce the effect of swath gaps
274 and cloud obscuration. The remaining data voids due to cloud cover or missing data were
275 subsequently filled using a linear temporal interpolation method, where a pixel was classified
276 as snow/land depending on the closest previous/next observation of snow/land.

277

278 **2.2.2. Agricultural data**

279

280 Two different grapevine varieties were selected to represent phenological patterns in the
281 valleys, namely: Flame Seedless (for table grapes) and Moscatel Rosada (for pisco grapes).
282 Phenological observations for these two varieties were carried out over a 10-year period
283 (2003–2012) at the *Instituto de Investigaciones Agropecuarias* (INIA), located a few
284 kilometers downstream from the catchment outlet. Grapevines were trained using an overhead
285 trellis system and fully irrigated during the whole growing season. The experiment kept track
286 of three major events: budburst (BB), full bloom (FB) and the beginning of harvest (HV).
287 Budburst was defined as the moment when the first leaf tips become visible and full bloom as
288 the moment when 80% of the flower caps are off. The beginning of harvest depends on the
289 intended use of the grapes. Table varieties require lower sugar contents ($\sim 16^\circ$ Brix) than
290 those dedicated to the production of pisco (22° Brix), which are generally harvested a few
291 months later [Ibacache, 2008].

292 A database of water access entitlements was used to estimate the total volume of water
293 licensed for abstraction in the catchment. This included a time series of monthly restrictions to
294 these entitlements issued by the *Dirección General de Aguas* during prolonged dry periods.

295

296

297 **3. Methods**

298

299 **3.1. Modeling framework**

300

301 In this paper we developed and compared three different models. These differed in their

302 approach to snowmelt and irrigation modeling. The first one, referred to as ‘Model A’, used a
303 simple degree-day approach to estimate snowmelt rates while neglecting the effects of
304 irrigation water-use (IWU) at the catchment scale. The second one, referred to as ‘Model B’,
305 ignored IWU effects just as Model A but relied on an enhanced degree-day approach to
306 account for the effects of net radiation and sublimation on melt rates. The third one, referred
307 to as ‘Model C’, used the same snowmelt routine as Model B and incorporated IWU effects
308 on natural streamflow using a conceptual irrigation module.

309 Figure 2 shows a block diagram of this modeling framework. The blue blocks refer to the
310 hydrological part of the framework shared by the three Models (see Sect. 3.1.2. and 3.1.3.).
311 The green blocks relate to the estimation of irrigation water requirements (IWR) used only by
312 Model C. This involves several phenological models to capture the main dynamics of crop
313 water needs over each growing season (Sect. 3.1.4.) and a moisture-accounting store
314 representing the valley soils (Sect. 3.1.3.). Net irrigation water-use at the catchment scale is
315 computed as a function of IWR, irrigated areas and water availability (i.e. natural streamflow)
316 (Sect. 3.1.3.). The whole modeling chain is fed by precipitation and temperature data.

317 We also stress that smoothing functions were used throughout this framework to remove
318 all threshold nonlinearities from the models’ equations (insofar as possible), as recommended
319 by several authors [e.g. Fenicia et al., 2011]. These smoothing functions will not be shown in
320 the following sections for the sake of clarity.

321

322 **3.1.1. Simplifying assumptions**

323

324 The modeling framework described in Fig. 2 relies on three important assumptions regarding
325 the representation of IWU and IWR at the catchment scale:

326

327 (1) First, IWU refers to the amount of water lost by evapotranspiration from the cropped
328 fields and the riparian vegetation that thrives along the irrigation canals. It should not
329 be confused with the actual surface-water withdrawals (SWW) that vary on a weekly
330 or monthly basis depending on historical water rights and planning/management
331 decisions. SWW include IWU but also non-consumptive losses caused by canal
332 seepage and deep percolation in the fields. Unfortunately, the impact of SWW on the
333 catchment behavior is difficult to estimate because reliable information on these
334 additional losses and the proportion of abstracted flows coming back to the system is

335 lacking. In this study, all return flows were assumed to come back to the river within
336 each 10-day time step. A similar assumption can be found in Kiptala et al. [2014].

337

338 (2) Second, IWR refer to the amount of water needed to satisfy crop evapotranspiration
339 under optimal conditions. In practice, this quantity depends on the irrigation technique
340 used by the farmers. In furrow-irrigated fields, IWR would be expected to bring the
341 soil moisture to saturation (or field capacity) and thereby satisfy crop water needs
342 during several days. In drip-irrigated fields, irrigation is required to compensate for the
343 difference between the amount of water stored in the soil and crop water needs. In this
344 study, we assumed that both irrigation techniques lead to the same water requirements
345 over a sufficiently long time interval.

346

347 (3) Third, the two varieties (Flame Seedless, Moscatel Rosada) selected to represent
348 phenological patterns in the valleys are at best a rough approximation of the real crop
349 diversity in this catchment. In reality, phenological dates for each type of grape (pisco
350 or table grapes) can spread over several days or weeks depending on the variety
351 involved. For instance, pisco producers report differences of between 1 and 2 weeks
352 between the various varieties used for pisco [Ibacache et al., 2010].

353

354 Taking heed of these underlying assumptions, all Models (A, B and C) were run at a daily
355 time step but evaluated using a 10-day time step. This 10-day interval was also more
356 consistent with the temperature-index approach used to estimate snowmelt rates [Hock, 2003]
357 (Sect. 3.1.2.).

358

359 **3.1.2. Snow accumulation and ablation modules**

360

361 The snow accumulation and ablation (SAA) modules developed in this study borrow much of
362 their philosophy and equations from the Cemanige model [Valéry et al., 2014]. The
363 catchment was divided into 5 elevation zones (EZ) of equal area, within which separate
364 modules operated simultaneously based on the same set of parameters. At each time step t ,
365 precipitation was partitioned into rain and snow by assuming a linear transition from snow to
366 rain across a fixed temperature range defined as $[-1^{\circ}\text{C}, 3^{\circ}\text{C}]$ [L'Hôte et al., 2005]. The
367 amount of water contained in the snowpack, or Snow Water Equivalent (SWE, in mm), was
368 then updated as:

$$SWE_t = SWE_{t-1} + Snow_t \quad (1)$$

369 As in the original Cemaneige model, an antecedent temperature index approach was used to
 370 keep track of the snowpack temperature (T_S , in °C) and determine when the pack was ready to
 371 melt:

$$T_{S,t} = \min[0, \theta_S T_{S,t-1} + (1 - \theta_S) T_{A,t}] \quad (2)$$

372 where T_A (°C) is the mean air temperature within the elevation zone and θ_S is a parameter
 373 quantifying the sensitivity of the snowpack temperature to T_A . As such, θ_S is expected to be
 374 higher in regions characterized by thick snowpacks (see also Sect. 4.2.1.). A similar
 375 representation can be found in other hydrological models, including enhanced versions of
 376 SWAT [Fontaine et al., 2002] and SRM [Harshburger et al., 2010]. . Melt rates (mm day^{-1})
 377 were computed as follows:

$$\text{Melt} = \begin{cases} \min[SWE, MF(T_A - T_{\text{thr}}) + Y_N/(\rho\lambda_f)] \times f(F_{\text{SCA}}) & \text{if } T_S = 0^\circ\text{C} \text{ and } T_A \geq T_{\text{thr}} \\ 0 & \text{if } T_S < 0^\circ\text{C} \text{ or } T_A < T_{\text{thr}} \end{cases} \quad (3)$$

$$\text{with } Y_N = \begin{cases} -C_T \times SWE \times \Delta T_S & \text{for Model A} \\ \Delta R_{\text{SW}} + \Delta R_{\text{LW}} - C_T \times SWE \times \Delta T_S & \text{for Models B and C} \end{cases} \quad (4)$$

$$f(F_{\text{SCA}}) = (1 - V_{\text{min}})F_{\text{SCA}} + V_{\text{min}} \quad (5)$$

$$F_{\text{SCA}} = \min[1, SWE/SWE_{\text{max}}] \quad (6)$$

378 where MF ($\text{mm } ^\circ\text{C}^{-1} \text{ day}^{-1}$) is the melt factor, T_{thr} is the temperature threshold at which
 379 snowmelt begins (usually set at 0°C), λ_f is the latent heat of fusion ($\sim 0.34 \text{ MJ kg}^{-1}$ at 0°C), ρ is
 380 the density of water ($\sim 1000 \text{ kg m}^{-3}$), ΔR_{SW} and ΔR_{LW} ($\text{MJ m}^{-2} \text{ day}^{-1}$) are the net shortwave and
 381 longwave radiations respectively (more details are given in the Appendix), C_T is the specific
 382 heat of snow ($\sim 0.0021 \text{ MJ kg}^{-1}$ at 0°C), F_{SCA} is the fractional snow-covered area and V_{min} is a
 383 parameter accounting for the effects of low SWE levels on melt rates. Y_N represents the
 384 energy available from net radiation and changes in the snowpack heat storage. The F_{SCA}

385 function can be thought of as a basic depletion curve representing the influence of snow
 386 distribution within each zone. As a first approximation, it was assumed to increase linearly
 387 with SWE until a threshold SWE_{max} was reached, above which the whole elevation zone was
 388 assumed to be covered by snow. Following Valéry et al. [2014], the value of SWE_{max} was
 389 fixed at 90% of the mean annual snowfall observed within each elevation zone separately.
 390 Similarly, the value of V_{min} was fixed at 0.1 as in the original Cemaneige model [Valéry et al.,
 391 2010b] to ensure that melt still occurred when F_{SCA} was close to zero. For Models B and C,
 392 sublimation losses (mm day^{-1}) were estimated as follows:

$$\text{Sublimation} = \begin{cases} 0 & \text{if } T_A \geq T_{thr} \\ \min[SWE, Y_N/(\rho\lambda_s)] \times f(F_{SCA}) & \text{if } T_A < T_{thr} \end{cases} \quad (7)$$

393 where λ_s is the latent heat of sublimation ($\sim 2.84 \text{ MJ kg}^{-1}$ at 0°C). Note that when $T_A \geq T_{thr}$ and
 394 $T_S < 0^\circ\text{C}$, all the energy available at the snow surface was used to warm the snowpack. The
 395 SAA module of Model A is equivalent to the Cemaneige model [Valéry et al., 2014] whereas
 396 that of Models B and C corresponds to an enhanced version of this model in which
 397 sublimation and net radiation are considered explicitly. However, both of these modules rely
 398 on the same calibrated parameters.

399

400 **3.1.3. Runoff production and routing modules**

401

402 Spatially-averaged rainfall and snowmelt estimates were combined into a single
 403 ‘precipitation’ term that was used as input to the lumped GR4J model [Perrin et al., 2003].
 404 Potential evapotranspiration (PE) was first determined for each grid cell using the
 405 temperature-based formula proposed by Oudin et al. [2005]:

$$PE_{\text{Oudin,C}} = \begin{cases} R_e(T_{A,C} + K_2)/(\rho\lambda_v K_1) & \text{if } T_A + K_2 > 0 \\ 0 & \text{otherwise} \end{cases} \quad (8)$$

406 where $T_{A,C}$ ($^\circ\text{C}$) is the interpolated air temperature of cell C, λ_v is the latent heat of
 407 vaporization ($\sim 2.46 \text{ MJ kg}^{-1}$) and K_1 (5°C) and K_2 (100°C) are fitted parameters (see Sect.
 408 3.1.4. for further details). Spatially-averaged PE inputs to the GR4J model (i.e. PE_{GR4J}) were
 409 obtained after subtracting the energy consumed by melting and sublimation:

$$PE_{GR4J} = \max \left(\sum_C PE_{Oudin,C}/N_C - \sum_Z (\lambda_f Melt_Z + \lambda_s Sublimation_Z)/(\lambda_v N_Z), 0 \right) \quad (9)$$

410 where N_C is the number of grid cells, N_Z is the number of elevations zones (Z), λ_v is the latent
 411 heat of vaporization ($\sim 2.46 \text{ MJ kg}^{-1}$) and $PE_{Oudin,C}$ (mm) is given by Eq. (11). Note that PE_{GR4J}
 412 accounts for evapotranspiration from soils, natural vegetation and crops only insofar as it
 413 relates to precipitation or meltwater. It is not supposed to include evapotranspiration from
 414 cultivated areas caused by irrigation water-use. Thus, the GR4J model simulates only those
 415 hydrological processes that relate to the ‘natural’ catchment behavior. Incorporation of IWU
 416 in the modeling framework does not modify the structure and governing equations of the
 417 GR4J model but only the estimates of natural streamflow. This choice can be justified by the
 418 fact that the cultivated areas concentrate mainly in the lower part of the catchment and
 419 represent only a small portion of the total area (Fig. 1).

420 The GR4J model was chosen for its simplicity and parsimony. Basically, the precipitation-
 421 runoff process is broken down into two components: a runoff generation module computes the
 422 amount of water available for runoff, i.e. ‘effective precipitation’, while a routing module
 423 subsequently routes this quantity to the catchment outlet. In the first module, a soil-moisture
 424 accounting (SMA) store is used to partition the incoming rainfall and/or snowmelt into
 425 storage, evapotranspiration and excess precipitation. At each time step, a fraction of the SMA
 426 store is also computed to represent soil drainage and added to excess precipitation to form the
 427 effective precipitation. The second module splits this quantity between two different pathways
 428 with respect to a constant ratio: 10% passes as direct runoff through a quick flow routing path
 429 based on a unique unit hydrograph whereas 90% passes as delayed runoff through a slow flow
 430 routing path composed of a unit hydrograph and an additional routing store. Outputs from
 431 both pathways are finally added up to simulate natural streamflow at the catchment outlet.
 432 This model relies on four calibrated parameters ($X1$, $X2$, $X3$ and $X4$) that are described in
 433 Table 1.

434

435 **3.1.4. Irrigation water-use module (Model C)**

436

437 In Model C, irrigation water requirements per unit area (IWR, in mm day^{-1}) were
 438 estimated for each crop variety i using a simple soil-water balance approach:

$$IWR_i = \max[0, ETM_i - SWC_i - P_{\text{valley}}] \quad (10)$$

$$\text{with } ETM_i(T_{A,V}) = K_{C,i}ET_0(T_{A,V}) \quad (11)$$

439 where ETM (mm day⁻¹) refers to crop evapotranspiration under optimal conditions and SWC
 440 (mm) to the average soil-water content in the root zone. P_{valley} (mm day⁻¹), ET₀ (mm day⁻¹)
 441 and T_{A,V} (°C) are respectively the areal effective precipitation, reference evapotranspiration
 442 and air temperature in the valleys, and K_C is a coefficient depending on crop growth stages. A
 443 realistic estimate of ET₀ was provided by using a modified version of Oudin's formula (Eq.
 444 (11)). In Oudin et al. [2005], the values of K₁ and K₂ were chosen as those giving the best
 445 streamflow simulations for different hydrological models applied to a large number of
 446 catchments. In this study, the FAO Penman-Monteith equation for a reference grass was used
 447 as a basis to re-calibrate these parameters at different locations across the valleys. This
 448 modification was required since the Penman-Monteith equation, which was more suited to
 449 estimating crop water needs, could not be used over the whole study period due to limited
 450 data availability (wind speed, relative humidity, solar radiation). Interpolated K_C curves were
 451 constructed for each crop variety using a series of phenological models to simulate the annual
 452 dates of budburst, full bloom, harvest and leaf fall (see Sect. 3.1.5.). The value of K_C at each
 453 of these dates (K_{C,BB}, K_{C,FB}, K_{C,HV} and K_{C,LF}) was determined from the literature [Villagra et
 454 al., 2014] and interviews with local grape growers. Net irrigation water-use in the catchment
 455 (IWU, in m³.s⁻¹) was computed as a function of IWR, irrigated areas and surface-water
 456 availability:

$$IWU = \begin{cases} \min \left[Q_{\text{nat}} - Q_{\text{min}}, \sum_i IWR_i \times A_i / \epsilon \right] & \text{if } Q_{\text{nat}} \geq Q_{\text{min}} \\ 0 & \text{otherwise} \end{cases} \quad (12)$$

457 where Q_{nat} (m³ s⁻¹) is the natural streamflow simulated by the GR4J model, ε is a conversion
 458 factor and A_i (ha) is the irrigated area for crop variety i, which varies on a yearly basis as
 459 shown in Fig. 1b. Q_{min} (m³ s⁻¹) is a minimum discharge below which no withdrawal is
 460 allowed. This parameter was fixed at 0.25 m³ s⁻¹ based on historical low-flow records.
 461 Simulated (influenced) discharge at the catchment outlet was computed from the difference

462 between Q_{nat} and IWU at each time step. When IWR could not be entirely satisfied, irrigation
 463 water was allocated to each crop variety i in proportion to its irrigated area:

$$AIW_i = \min[IWR_i, \epsilon \times IWU \times A_i/A_{tot}^2] \quad (13)$$

464 where AIW_i (mm) is the amount of water allocated to crop variety i and A_{tot} (ha) is the sum of
 465 all irrigated areas. Finally, the average soil water-content in the root zone was updated as:

$$SWC_{i,t} = \max[0, SWC_{i,t-1} + P_{Valley,t} + AIW_{i,t} - ETM_{i,t}] \quad (14)$$

466

467

468 **3.1.5. Phenological modeling (Model C)**

469

470 To construct the K_C curves, the growing season was split into five phenophases:
 471 endodormancy, ecodormancy, flowering, ripening and senescence. For each grapevine
 472 variety, different process-based models were applied to predict the start and end dates of each
 473 phenophase (Fig. 3).

474 A simplified version of the UniChill model [Chuine, 2000] was chosen to simulate the
 475 annual dates of budburst (t_{BB}). This model covers the periods of endodormancy, when growth
 476 inhibition is due to internal physiological factors, and ecodormancy (or quiescence), when
 477 buds remain dormant because of inadequate environmental conditions. To emerge from
 478 endodormancy, grapevines usually require an extended period of low temperatures, which is
 479 represented in the model as an accumulation of ‘chilling’ rates R_{CH} :

$$C_{BB} = \sum_{t=t_0}^{t_1} R_{CH}(T_{A,V}) \quad (15)$$

$$R_{CH}(T_{A,V}) = 1/\left[\delta \left(1 + e^{a(T_{A,V}-b)^2}\right)\right] \quad (16)$$

480 where $T_{A,V}$ is the average daily temperature in the valley and t_0 , a , b and C_{BB} are fitted
 481 parameters described in Table 1. δ is a scaling factor set at 0.5 to ensure that the optimal
 482 chilling rate (when $T_{A,V} = b$) has a value of 1 [Caffarra and Eccel, 2010]. A sensitivity analysis
 483 (not shown here for brevity's sake) was performed to determine the optimal value for t_0 , i.e.
 484 the starting date of the endodormancy period (see Table 1). Likewise, from dormancy release
 485 to budburst an extended period of high temperatures is generally required (ecodormancy).
 486 This process is represented as an accumulation of 'forcing' rates R_{BB} :

$$F_{BB} = \sum_{t=t_1}^{t_{BB}} R_{BB}(T_{A,V}) \quad (17)$$

$$R_{BB}(T_{A,V}) = 1/[1 + e^{c(T_{A,V}-d)}] \quad (18)$$

487 where c , d and F_{BB} are fitted parameters. To prevent over-parameterization, the values of c
 488 and d were fixed at -0.25 and 15°C based on information available in the literature [Caffarra
 489 and Eccel, 2010; Fila et al., 2012]. The sigmoid function of Eq. (21) describes the temperature
 490 dependence of growth rates in a more realistic way than usual approaches based on growing
 491 degree-days.

492 The 4-parameter model developed by Wang and Engel [1998] (hereafter referred to as
 493 WE) was selected to simulate the annual dates of full bloom (t_{FB}) and harvest (t_{HV}):

$$F_{FB} = \sum_{t=t_{BB}}^{t_{FB}} R_{FB}(T_{A,V}) \quad \text{and} \quad F_{HV} = \sum_{t=t_{FB}}^{t_{HV}} R_{HV}(T_{A,V}) \quad (19)$$

$$R_{FB}(T_{A,V}) = R_{HV}(T) \quad (20)$$

$$= \begin{cases} \frac{2(T_{A,V} - T_{min})^\alpha (T_{opt} - T_{min})^\alpha - (T_{A,V} - T_{min})^{2\alpha}}{(T_{opt} - T_{min})^{2\alpha}} & \text{if } T_{min} \leq T_{A,V} \leq T_{max} \\ 0 & \text{otherwise} \end{cases}$$

$$\text{with } \alpha = \log(2)/\log[(T_{max} - T_{min})/(T_{opt} - T_{min})] \quad (21)$$

494 where F_{FB} , F_{HV} and T_{opt} (°C) were calibrated separately for each variety. Note that T_{opt} also
 495 varies with the phenophase under study (flowering or ripening). Compared to other flowering
 496 and harvest models based on forcing rates, this one has the major advantage of also

497 accounting for the inhibiting effect of extreme temperatures on photosynthesis. As leaf growth
498 typically ceases at temperatures below 0–5°C [Hendrickson et al., 2004] and above 35–40°C
499 [Greer and Weedon, 2013], parameters T_{\min} and T_{\max} were fixed beforehand at 0°C and 40°C
500 respectively [García de Cortázar-Atauri et al., 2010].

501 Eventually, the post-harvest period was modeled as a constant number of days (N_{LF})
502 between t_{HV} and the end of leaf fall (t_{LF}). The value of N_{LF} was obtained from interviews with
503 local grape growers for each variety (see Table 1).

504

505 **3.2. Model evaluation**

506

507 The phenological and hydrological models were evaluated separately using different methods
508 and/or objective functions. Models A and B have the same number of calibrated hydrological
509 parameters (i.e. 6 parameters).

510

511

512

513 **3.2.1. Hydrological modeling**

514

515 The dataset was divided into a calibration period (1985–1995), showing a sharp increase in
516 irrigated areas (+100%), and a validation period (1995–2005), characterized by a much lower
517 increase (+20%) (Fig. 1b). Each period was defined in terms of water years (from May 1 to
518 April 30) and included at least one major El Niño (1987–88, 1997–98 and 2002–03) or La
519 Niña (1988–89, 1998–99 and 1999–00) event.

520 The models were evaluated using either (1) simulations obtained with a single, ‘optimal’
521 parameter set, or (2) probabilistic predictions obtained by sampling the posterior distributions
522 of the parameters. In the first case, model efficiency and internal consistency were assessed.
523 In the second case, predictive uncertainty bands were derived and scrutinized in terms of
524 reliability and sharpness.

525

526 ***Model efficiency and internal consistency***

527 Model efficiency measures the ability to fit the observed behavior of the system with regard to
528 specific criteria. In this study, the Shuffle Complex Evolution (SCE) algorithm [Duan et al.,
529 1993] was used to maximize the following criterion:

$$F_{obj} = (KGE + KGE_{inv})/2 \quad (22)$$

530 where KGE and KGE_{inv} refer to the Kling-Gupta Efficiency [Gupta et al., 2009] computed
 531 from discharge (Q) and inverse discharge (1/Q) values respectively. This composite criterion
 532 was chosen to emphasize high and low flows equally [Pushpalatha et al., 2012; Nicolle et al.,
 533 2014].

534 Internal consistency can be defined as the ability to reproduce the dynamics of internal
 535 catchment states without conditioning the model parameters on additional data. Here, this
 536 analysis was limited to the Snow Accumulation and Ablation module to evaluate its ability to
 537 reproduce the seasonal pattern of snow storage and release within each elevation zone. This
 538 was achieved through visual inspection of model-based and MODIS-derived F_{SCA} time series
 539 and based on the snow error criterion defined in Hublart et al. [2015].

540

541

542

543 *Model predictive uncertainty*

544 The Differential Evolution Adaptive Metropolis (DREAM) algorithm [Vrugt et al., 2009] was
 545 chosen to approximate the posterior distributions of model parameters and obtain probabilistic
 546 streamflow predictions. This required a statistical model of the differences between observed
 547 and simulated flows (i.e. residual errors). We used the Generalized Likelihood (GL) function
 548 introduced by Schoups and Vrugt [2010], which describes correlated, heteroscedastic and
 549 non-gaussian errors based on a number of parameters given in Table 1. Uniform priors were
 550 assumed to reflect the lack of information on model parameters in this catchment. After a
 551 maximum of 30,000 iterations, the quantitative diagnostic of Gelman and Rubin [1992] was
 552 used to determine when the chains had converged to the stationary posterior distribution.

553 The reliability of the predictive distributions was first assessed by checking for the ability
 554 of various p -confidence intervals (with $p = 0.05$ to 0.95) to bracket the adequate percentage of
 555 streamflow observations (hereafter called POCI for Percentage of Observations within the p -
 556 Confidence Interval):

$$POCI(p) = N(Q_{obs} \in [Limit_{Upper}(p), Limit_{Lower}(p)] \forall t) / n \quad (23)$$

557 where n is the total number of observations, $\text{Limit}_{\text{Upper}}(p)$ and $\text{Limit}_{\text{Lower}}(p)$ are the upper and
 558 lower boundary values of the p -confidence interval and N indicates the number of
 559 observations enclosed within these boundaries. When plotted as a function of p , the POCI
 560 points should fall along the diagonal 1:1 line. The predictive distributions were also verified
 561 using the Probability Integral Transform (PIT) values of streamflow observations, defined as
 562 [e.g. Thyer et al., 2009; Wang et al., 2009; Engeland et al., 2010]:

$$\pi_t = F_t(Q_{\text{obs},t}) \quad (24)$$

563 where F_t is the empirical cumulative distribution function (CDF) of streamflow predictions at
 564 time t . For ideal predictions (i.e. based on correct statistical assumptions regarding model
 565 errors), the π_t values are expected to be uniformly distributed between 0 and 1. More details
 566 on the correct use and interpretation of PIT plots, including the use of Kolmogorov
 567 significance bands as a test of uniformity, can be found in Laio and Tamea [2007] (see also
 568 Fig. 4).

569 Finally, the sharpness (or ‘resolution’) of the predictive distributions was measured using
 570 the Average Relative Interval Length (ARIL) criterion proposed by Jin et al. [2010], which
 571 should be as small as possible for any p between 0 and 100%:

$$\text{ARIL}(p) = \frac{1}{n} \sum_t [\text{Limit}_{\text{Upper},t}(p) - \text{Limit}_{\text{Lower},t}(p)] / Q_{\text{obs},t} \quad (25)$$

572 Each of these posterior diagnostics (POCI, PIT and ARIL) was performed separately for all
 573 streamflow observations and three distinct regions of the observed flow duration curve,
 574 namely: high-flows (20% exceedance probability), mid-flows (20 to 80% exceedance
 575 probability) and low-flows (20% exceedance probability).

576

577 **3.2.2. Phenological modeling**

578

579 The phenological models used in Model C were calibrated by minimizing the root-mean-
 580 square error (RMSE) between simulated and observed phenological dates over the whole
 581 dataset (2003–2013). This was achieved using the SCE algorithm with the same number of
 582 complexes for all models and crop varieties. Given the small number of available
 583 observations, a leave-one-out cross-validation technique was chosen to assess the robustness

584 of each model. Additional metrics such as the Nash-Sutcliffe Efficiency (NSE) and the mean
585 difference between observed and predicted dates (i.e. model bias) were also used in validation
586 to characterize the modeling errors. On the whole, 8 parameters required calibration for each
587 variety (Table 1).

588

589

590 **4. Results**

591

592 **4.1. Phenological simulations**

593

594 Figure 5, Table 2 and Table 3 show the results obtained for both grapevine varieties with the
595 three phenological models. On the whole, approximately 76% of the differences between
596 observed and predicted phenological dates fell within the range of ± 5 days during
597 calibration (Fig. 5). Moreover, mean absolute errors did not exceed 6.4 days in any case. Such
598 errors can be considered acceptable with regard to the 10-day time step chosen to evaluate the
599 hydrological models.

600 The best results were obtained for Flame Seedless with the budburst (BB) model and for
601 Moscatel Rosada with the full bloom (FB) and harvest (HV) models. RMSE values ranged
602 from 3.0 to 6.1 days in calibration and from 5.4 to 7.9 days in validation, indicating a
603 moderate loss of performance (Table 2). In general, bias values remained close to zero, except
604 for Moscatel Rosada with the HV model. NSE values were positive for all varieties and
605 models in calibration but decreased sharply in validation, with only two values above 0.50
606 and one negative value for Flame Seedless with the FB model. However, very low to negative
607 NSE values are not uncommon in phenological modeling when only a few observations (< 10
608 years) collected from a single site are used to calibrate the models [e.g. Parker et al., 2013].
609 The optimized parameter values displayed in Table 3 are discussed in Sect. 5.4.

610

611 **4.2. Hydrological simulations**

612

613 **4.2.1. Model efficiency and internal consistency**

614

615 Table 4 show the results obtained from the calibration and validation of Models A, B and C.
616 Clearly, Model C was found to perform better than Models A and B with respect to the

617 objective function given by Eq. (25). This higher performance was mostly the result of
618 improved low-flow simulations (KGE_{inv}). Table 5 shows that simulated sublimation rates and
619 contribution to snow ablation remained approximately the same when IWU was introduced in
620 the model equations. Estimated mean annual sublimation rates at high elevations (EZ no. 4
621 and 5) were consistent with those found by other studies, including experimental studies
622 conducted on small glaciers of the region [MacDonell et al., 2013].

623 The internal consistency of the SAA module was verified over an independent validation
624 period (2000–2011) using the parameters (θ_s , MF) calibrated with each Model from 1985 to
625 1995. The snow errors displayed in Table 4 vary from 2% in the first elevation zone (EZ no.
626 1) to 11–17% in the last one (EZ no. 5). Such errors were very encouraging, as they were
627 comparable to those obtained by Hublart et al. (2015) in the same catchment with less
628 parsimonious (and less realistic) snowmelt models. The impact of considering net radiation
629 and sublimation in the model equations, however, was only evident for EZ no. 4 and 5, where
630 a moderate drop in the snow error was observed. Model A even performed slightly better than
631 Model B with respect to the F_{obj} function.

632 Figure 6 provides a visual comparison of simulated and observed fractional snow-covered
633 areas (F_{SCA}) during this validation period for Model C. On the whole, it can be seen that the
634 SAA model did not accumulate snow from one year to another, which was consistent with the
635 observed inter-annual pattern of snow cover in the catchment. However, there were important
636 discrepancies between the lower and upper elevation zones. In the lower zones (EZ no. 2 and
637 3), the model did fairly well during several years of the period (e.g. 2001, 2004, 2009 and
638 2010) but also under-estimated the annual snow cover duration (SCD) during several other
639 years (e.g. 2002, 2003 and 2007). In the upper zones (EZ no. 4 and 5), the model generally
640 failed to reproduce the observed variations in F_{SCA} despite improved estimates of the annual
641 SCD. In EZ no. 5, there was also a tendency to over-estimate the SCD during the last 3–4
642 years of the period.

643

644 **4.2.2. Model predictive uncertainty**

645

646 Between 10 000 and 13 000 model evaluations were required to reach convergence to a
647 limiting distribution depending on the Model used. In each case, the last 5 000 samples
648 generated with DREAM were used to compute the posterior diagnostics presented in Sect.
649 3.2.1. and generate predictive uncertainty bands.

650

651 Figure 7 provides a range of formal tests of the statistical assumptions made to describe
652 model residuals in the case of Model C. The density plot of Fig. 7a confirms that model
653 residuals were broadly symmetric and kurtotic, although kurtosis appears to be slightly
654 overestimated. Heteroscedasticity (Fig. 7c) was largely removed by the variance model of the
655 GL function. However, Fig. 7b shows that the assumption of independence was not fully
656 respected, as residuals remained slightly correlated (0.35) at a lag of 1 and at some greater
657 lags, indicating potential storage errors in the model structure.

658

659 Figure 8 displays the scatter plots and posterior histograms of hydrological parameters for
660 Models A and C. The results obtained with Model B are not shown here as they were
661 generally close to those of Model C. As can be seen, differences between the structures of
662 Models A and C had no particular effect on parameter identifiability. All parameters appeared
663 to be relatively well-defined with approximately Gaussian distributions, although the values
664 of θ_s , MF and $X3$ occupied a wider range of their prior intervals with Model A than with
665 Models B and C. Introducing sublimation and net radiation in the SAA module reduced the
666 correlation between θ_s and MF observed with Model A but simultaneously increased the
667 interaction of θ_s with $X3$ and $X4$. Likewise, additional checks performed with Models B and C
668 showed that the incorporation of irrigation water-use in Model C led to a strong correlation
669 between $X2$ and $X3$, which questions the internal consistency of the Runoff production and
670 routing module when increasing the model complexity..

671

672 Figure 9 shows the posterior diagnostics used to evaluate the reliability (PIT, POCI) and
673 resolution (ARIL) of forecast distributions for Models B and C. At first sight, the PIT values
674 obtained with all streamflow observations appear to be distributed quite uniformly during
675 both simulation periods. Small departures from the diagonal line and the 5% Kolmogorov
676 confidence bands indicate a tendency to under-predict the observed data, but this applies to
677 both models, especially in validation. On the contrary, significant differences between the two
678 models become obvious when looking at specific portions of the observed flow duration
679 curve. At low flows, the PIT values obtained with Model B revealed a significant over-
680 prediction bias during both calibration and validation periods. While it did not affect the
681 percentage of observations covered by the confidence intervals (as POCI values remained
682 close to the diagonal line), this systematic bias resulted in very high ARIL values (exceeding
683 1.5 in calibration and 3 in validation with the 95% confidence intervals). By contrast, Model
684 C slightly over-estimated predictive uncertainty in calibration but led to highly reliable low-

685 flow predictions in validation, as evidenced by the PIT and POCI plots. This resulted in
686 relatively low ARIL values (< 1). At mid-flows, the two models exhibited a similar behavior
687 characterized by a systematic under-prediction bias, under-estimated POCI values and
688 relatively low ARIL values (< 1). At high flows, the PIT values were well within the
689 Kolmogorov confidence bands for both models, although there was still a tendency to under-
690 predict the observed data. In validation, this under-prediction bias translated into an
691 excessively low number of observations enclosed within any p -confidence interval for $p >$
692 70%.

693
694 Figure 10 shows the uncertainty bands obtained with Models B and C during the two
695 simulation periods. The dark blue region represents the uncertainty in streamflow predictions
696 associated with the posterior parameter distributions while the light blue region represents the
697 total uncertainty arising from parameter, model structure and input errors simultaneously.
698 Some portions of the observed hydrograph have been enlarged to highlight key differences
699 between the two models. In general, uncertainty bands should be wide enough to include the
700 expected percentage of streamflow observations (here, 95%), but not so wide that the
701 representation of the observed hydrograph becomes meaningless. From this perspective, the
702 main differences between Models B and C were observed for summer flows, i.e. during the
703 irrigation season. Model B results in large uncertainty bands that are able to capture most of
704 the observations but which fail to reproduce the seasonal pattern of streamflow during dry
705 years (e.g. 1989–90, 1994–95, 1996–97, 1997–98, 1999–00). In this case, structural and input
706 errors represent the dominant sources of uncertainty. By contrast, the width of the prediction
707 limits obtained with Model C tends to decrease as the magnitude of the predicted streamflow
708 decreases. In this case, parameter uncertainty accounts for most of the predictive uncertainty
709 during summer. However, winter and early summer flows are often under-predicted by both
710 models. This last point is further discussed in Sect. 5.3.

711

712

713 **5. Discussion**

714

715

716

717 **5.1. Snow accumulation and ablation**

718

719 The ‘optimal’ cold-content factor (θ_s) was very close to 1 with all Models (Fig. 7),
720 indicating a relative insensitivity of the snowpack temperature to changes in air temperature.
721 This finding seems a contradiction of the idea that shallow snow packs such as those observed
722 in the region should have a low thermal inertia. By comparison, Stehr et al. [2009] obtained a
723 value of zero for θ_s after calibrating the SWAT model in a snowmelt-fed catchment of the
724 more humid Central Chile (38°S). One possible explanation for this apparent contradiction is
725 that mean daily temperatures in North-Central Chile are rarely negative at low and mid-
726 elevations (< 4000 m a.s.l.). A high value of θ_s was therefore required to preserve the
727 seasonality of melting during the spring and summer months, despite small snow depths and
728 frequently positive air temperatures throughout the winter. In EZ no. 3 and 4, this model
729 requirement may be due to the impact of latent heat fluxes on the snowpack cold-content.
730 During the winter, almost all the energy available from net radiation and sensible heat
731 transfers is consumed by sublimation. This maintains the snowpack temperature slightly
732 below 0°C and effectively delays snowmelt until the mean daily air temperature stabilizes
733 above 0°C for a sufficiently long period of time. Another possible explanation is that a high
734 value of θ_s implicitly accounts for the effect of night-time freezing, which further delays
735 snowmelt despite warm day-time temperatures. At high elevations (> 4000 m a.s.l., i.e. EZ no.
736 5), where observed air temperatures are mostly negative, we note that a constant lapse rate of
737 6.0°C km⁻¹, as applied in this study for all elevation zones, was also likely to over-estimate
738 temperature inputs. Lapse rates at these elevations are generally much greater than that, being
739 in fact closer to the dry adiabatic lapse rate. Again, this would be expected to generate high
740 values of θ_s to compensate for temperature over-estimation.

741 The main drawback of this approach (i.e. using air temperature as a proxy for the
742 snowpack cold-content) is that it remains largely implicit and only indirectly connected to the
743 amount of water lost by sublimation in the model (i.e. the outcome of Eq. (10) has no effect
744 on Eq. (2)). This does not mean, however, that a physically-oriented interpretation cannot be
745 sought *a posteriori* to check for the model realism. Alternative approaches can also be used to
746 account for the delay in meltwater production at the start of the ablation season. In general,
747 these will involve an additional store representing the water-holding capacity of the snowpack
748 [Schaepli and Huss, 2011]. Although further research would be required to compare the
749 relative merits of each approach, the representation chosen in this study may be more suited to
750 catchments with shallow snowpacks and significant sublimation.

751 The ‘optimal’ melt factor (MF) was significantly higher with Model A than with Models B
752 and C (Fig. 7). This was not surprising since, in the case of Models B and C, the effects of net
753 radiation were explicitly considered and the melt factor was meant to parameterize only the
754 contribution of turbulent energy fluxes. Such a ‘restricted’ melt factor is expected to increase
755 with increasing wind speed and/or relative humidity, as shown by Brubaker et al. [1996]. The
756 relatively low values ($\sim 2 \text{ mm } ^\circ\text{C}^{-1} \text{ day}^{-1}$) obtained here were therefore consistent with the
757 overall dry conditions of the study area. However, we found little evidence of improved
758 model performance and internal consistency when a restricted melt factor was used and net
759 radiation and sublimation were introduced in the model equations (see Table 4). This lack of
760 sensitivity may be due to other sources of uncertainty, in particular regarding the choice of an
761 adequate snow depletion curve to estimate fractional snow-covered areas (Eq. (6)).

762 While most snowmelt routines used in conceptual catchment models assume either
763 entirely snow-free or entirely snow-covered elevation zones, accounting for the proportion of
764 each zone over which snow extends can be critical where mean snow depths are known to be
765 small. As a first approximation, we relied on a linear relationship between SWE and F_{SCA} that
766 did not account for wind redistribution effects or differences in radiation receipt caused by
767 slopes of different aspects. In the dry Andes, wind-induced redistribution has been shown to
768 significantly increase the spatial variability in snow depth, hence reducing the total snow
769 cover area during winter [Gascoïn et al., 2013; Ayala et al., 2014]. For a proper assessment of
770 predictive uncertainty, a multi-criteria likelihood function accounting for the differences
771 between several types of simulated and observed responses (typically, fractional snow-
772 covered areas and stream flows) should be used [e.g. Koskela et al., 2012]. This is the subject
773 of ongoing research.

774

775 **5.2. Runoff generation and routing**

776

777 Figures 9 and 10 revealed a clear under-prediction bias in the simulation of winter and early
778 spring flows during several water years. Further details on these systematic deficiencies are
779 provided by Fig. 11, which focuses on a specific El Niño event (2002–03). From May to
780 September 2002, the observed winter flow increased rapidly from 0.15 to 0.5 mm day^{-1} (Fig.
781 11a) in response to intense rainfall events (Fig. 11b) and gradual snowmelt (Fig. 11c). Most of
782 this precipitation, however, served to refill the soil-moisture accounting (SMA) store of the
783 model, which, after three years of intense La Niña-related drought (1999–2002), was only
784 15% of capacity (Fig. 11d). As a result, effective precipitation did not exceed 0.5 mm day^{-1}

785 during this five-month period (Fig. 11e), of which only 10%, i.e. less than 0.05 mm day^{-1} ,
786 were processed through the quick flow routing path (Fig. 11f). The remaining 0.45 mm day^{-1}
787 were added to the routing store, whose water level was also very low in May 2012. The
788 overall quantity routed by both pathways was therefore largely insufficient to match the actual
789 streamflow. A similar sequence was observed for all water years characterized by the same
790 failures in streamflow predictions, shedding light on two critical sources of uncertainty related
791 to structural deficiencies and input data errors.

792

793

794 **5.2.1. Structural deficiencies**

795

796

797

798

799 One possible source of model inadequacy lies in the representation of runoff production
800 by a single SMA store, which lumps together quite distinct landscape units. In the mountains,
801 most of the land cover is dominated by barren to sparsely vegetated exposed rocks, boulders
802 and rubble. The topography is steep, with slopes as large as 30° and very poor soil
803 development above the mountain front zone. By contrast, the valley bottoms appear as
804 relatively flat areas largely covered by vegetation. Alluvial fans are also found along the
805 mountain foothills, acting as hydrologic buffers between the mountain blocks and the valleys.

806 Another potential source of structural uncertainty relates to the type of precipitation
807 entering the SMA store. Snowmelt typically occurs at a much lower and more consistent rate
808 than rainfall, and much of the meltwater is expected to soak into the ground. Rain, while not a
809 dominant feature of semi-arid Andean catchments, can exert a significant influence on winter
810 flows even during dry years. While snowmelt events occur mainly in the uplands, most
811 rainfall events take place in the valley bottoms, i.e. much closer to the catchment outlet and
812 generally not very far from the saturated riparian zone. In most precipitation-runoff models,
813 however, rainfall and snowmelt inputs are treated as the same kind of ‘water’ and processed
814 through the same model paths. More research is needed to determine whether different types
815 of precipitation inputs, which would be expected to involve different modes of runoff
816 generation, should translate into different model representations. Investigating such
817 hypotheses was far beyond the scope of this study.

818

819

820

5.2.2. Impacts of input data errors

821

822 Relatively high values were obtained for $X1$ (> 1000 mm) and $X2$ ($\sim 4\text{--}5$ mm), which was
823 somewhat surprising given our understanding of storage capacities and water fluxes in the
824 Claro River catchment. The $X2$ parameter, in particular, is used to represent groundwater
825 exchanges with the underlying aquifer and/or neighboring catchments. Positive values
826 indicate a net water gain at the catchment scale whereas negative values relate to a net water
827 loss. Le Moine et al. [2007] have shown from the analysis of 1040 French catchments that
828 alluvial aquifers are more likely to be associated with negative values of $X2$ whereas
829 crystalline bedrocks tend to correlate with values centered on zero ($-5 < X2 < 5$). Over the
830 long term, however, the value of $X2$ is expected to be zero if the catchment is a closed system.

831 In this catchment, the valley-fill aquifers that compose most of the groundwater flow
832 system are bounded by large mountain blocks of granitic origin, which drastically limits inter-
833 catchment flow paths. Ground water in the bedrock is typically found in fractures or joints,
834 with a low storage capacity, and soils are, on the whole, poorly developed. As a result, low
835 values of $X1$ and negative values of $X2$ would have seemed more 'realistic'. Note that the
836 autocorrelation structure of model residuals shown in Fig. 7 was also indicative of substantial
837 storage errors in the hydrological model. This lack of physical realism suggests that other
838 factors may be at play. Both of these parameters, indeed, are known to interact strongly with
839 precipitation and evapotranspiration input errors [e.g. Andréassian et al., 2004; Oudin et al.,
840 2006; Thyer et al., 2009]. The capacity of the SMA store tends to increase in the presence of
841 random precipitation errors or if precipitation is systematically over-estimated [Oudin et al.,
842 2006]. Likewise, an excessively high value of $X2$ might indicate that potential
843 evapotranspiration is over-estimated and/or precipitation under-estimated.

844 As in many mountainous catchments, some precipitation events occurring at high
845 elevations may not be captured by the gauging network ($< 3\ 200$ m a.s.l.) used to interpolate
846 precipitation across the catchment. These occasional errors naturally add to systematic
847 volume errors caused by wind, wetting and evaporation losses at the gauge level, leading to an
848 overall underestimation of precipitation at the catchment scale. However, a large uncertainty
849 also surrounds the estimation of elevation effects on precipitation. Mean annual precipitation
850 was assumed to increase by ~ 0.4 m w.e. km^{-1} (Sect. 2.2.1.), yet in the absence of reliable
851 precipitation data above 3 200 m a.s.l., it is unclear whether this gradient under-estimated or
852 over-estimated precipitation enhancement. In general, it is unlikely that a constant value

853 would represent orographic effects correctly at all elevations and over the whole simulation
854 period. Precipitation enhancement in the Andes can vary considerably on a year-to-year basis
855 or from one event to another [Falvey and Garreaud, 2007], leading to time-varying errors in
856 the estimation of precipitation inputs. From Fig. 6 we hypothesize that precipitation was on
857 the whole underestimated, and only occasionally overestimated. Overestimation of potential
858 evapotranspiration is also a plausible hypothesis for Models B and C owing to possible
859 interactions with the estimation of sublimation rates and irrigation water-use (Fig. 7).

860

861

862

863 **5.3. Phenological modeling**

864

865 Contrary to lumped catchment models, the phenological models used in this study allow for a
866 direct interpretation of parameter values through comparison with existing experimental
867 studies. This provides a second level of model validation.

868 The values obtained for T_{opt} (i.e. the optimal forcing temperature) with the full bloom and
869 harvest models (Table 3) were generally close to the range of optimal photosynthetic
870 temperatures reported in the literature, i.e. typically 20–30°C [García de Cortázar-Atauri et
871 al., 2010]. On the contrary, relatively high values (around 11–12°C) were found for parameter
872 b (i.e. the optimal chilling temperature) compared to those reported by previous modeling and
873 experimental [e.g. Fila et al., 2012] studies. Moreover, the values obtained for parameter a ,
874 which determines the range of acceptable chilling temperatures around the optimum b , imply
875 that temperatures around 13–16°C were still effective as chilling temperatures. Caffarra and
876 Eccel [2010] and Fila et al. [2014] also found large effective chilling intervals with similar
877 budburst models but different grapevine varieties, which they explained in different ways. In
878 our case, this outcome was most likely related to the use of mean daily temperatures as inputs
879 to the budburst model. Very high diurnal variations (~20°C) can be observed at the INIA
880 experimental site, where a mean temperature of 11–12°C actually reflects temperatures close
881 to 0°C during several hours of the day. The critical states of chilling (C_{BB}) obtained for both
882 varieties indicate that between 11 and 27 days at 11–12°C were required to break
883 endodormancy. Assuming that winter temperatures remained close to zero during at least 5
884 hours per day, these results are fully consistent with the fact that most grapevine varieties
885 typically require between 50 and 400 hours at temperatures below 7°C to achieve budburst
886 [Fila et al., 2012]. However, given the limited number of years with available observations

887 and the absence of direct evidence for the release of endodormancy, possible trade-offs
888 between the chilling (a , b , C_{BB}) and forcing (F_{BB}) parameters during the optimization process
889 cannot be dismissed *a priori*. Thus, while the phenological models can be considered reliable
890 under the conditions observed over 1985–2005, their results should be treated very carefully
891 when dealing with potential impacts of higher temperatures.

892

893

894

895 **5.4. Irrigation water-use modeling**

896

897 While no ground data was available to verify our estimates of irrigation water-use, a
898 comparison was made with net surface-water withdrawals (SWW) estimated from the water
899 access entitlements database (Fig. 12). Not surprisingly, this comparison revealed large
900 discrepancies between these two quantities, especially from 1985 to 1990, which could
901 explain the poor performance of all Models in water years 1985–86 and 1986–87 (Fig. 10). It
902 is worth noting, however, that SWW data reflect more a level of water availability in the
903 catchment than the actual water consumption in the vineyards. These data may also indicate
904 sudden changes in the management of water resources at the regional scale which do not
905 necessarily affect irrigation requirements at the local scale. Overall, the actual water-use in the
906 catchment is likely to be somewhere between simulated IWU and net SWW estimates.
907 Incorporating IWU simulations into conceptual catchment models can help reduce the
908 uncertainty associated with low-flow simulations, yet it is by no means a substitute for
909 accurate measurement of water withdrawals.

910 The relative stability of simulated IWU from year to year is perhaps more surprising given
911 the complexity of the phenological models used. However, this stability could not be taken for
912 granted before running the models (it can only be observed *a posteriori*). Using phenological
913 models also has considerable advantages in terms of model robustness under climate- and/or
914 human-induced changes, which are further discussed in Section 6.

915

916

917

918

919

920 **6. Conclusion and prospects**

921

922 Hydrological processes are often poorly defined at the catchment scale due to the limited
923 number of observations at hand and the integral (low-dimensional) nature of these signals
924 (e.g. streamflow). This makes it relatively easy to over-fit the data by adding new hypotheses
925 to our models, leading to a low degree of *falsifiability* from a Popperian perspective.
926 Therefore the incorporation of new processes into a given model structure should be achieved
927 using as less additional parameters as possible and the same level of mathematical abstraction
928 as in the original model (as stated in Section 1.4). Ultimately, it is also necessary to show that
929 this increase in model complexity improves hydrological simulations without increasing
930 predictive uncertainty.

931

932 In the present paper, sublimation losses were incorporated by assuming that the snowpack
933 can either melt or sublimate. This modeling choice may seem to oversimplify the physics of
934 snowpacks, yet it allows for the same level of process representation as in commonly-used
935 empirical melt models. On the whole, this modification helped to reduce errors in the
936 simulation of snow-cover dynamics at high elevations without increasing the number of
937 snow-related parameters. However, more research is needed to determine the exact interaction
938 between snow sublimation and melt in the model. Compared to sublimation losses, the
939 introduction of irrigation water-use (IWU) increased the overall number of parameters. Yet
940 this increase in complexity came with additional data (observed phenological dates) to reduce
941 the number of degrees of freedom. The reliability of probabilistic streamflow predictions was
942 greatly improved when IWU was explicitly considered, resulting in relatively narrow
943 uncertainty bands and reduced structural errors. As such, this model modification appears to
944 be supported by the available data. Incidentally, this approach also provided evidence that
945 water abstractions from the unregulated Claro River is impacting on the hydrological response
946 of the system.

947

948 One of the main advantages of incorporating IWU is that it provides an estimate of natural
949 streamflow which can be used to assess the system's capacity to meet increasing irrigation
950 needs [e.g. Fabre et al., 2015b]. To our knowledge, most of the other approaches used to
951 'naturalize' influenced streamflow in agricultural catchments do not account for the impacts
952 of climate variability on crop water-use. Instead, the sum of all historical water rights is

953 usually taken as an upper bound for the actual water consumption and added back to observed
954 streamflow *before* calibrating the model. This makes it difficult to use conceptual catchment
955 models in climate change impact studies, since changes in temperature patterns are expected
956 to affect both the timing and volume of irrigation water-use. Depending on their magnitude,
957 seasonal shifts in the timing of snowmelt runoff and phenological events could result in either
958 additive or countervailing effects. Earlier peak flows, for instance, could lead to an increase in
959 water supply at a time when it is not required, or simply compensate for a similar shift in crop
960 phenology. A new generation of low-dimensional modeling approaches is required to better
961 understand how these processes interact and evaluate the possibility of selecting the most
962 suitable varieties and irrigation strategies for a given hydro-climatic context [Duchêne et al.,
963 2010b; Palliotti et al., 2014]. In this paper, the use of phenological models based on functions
964 that integrate both the negative and positive effects of higher temperatures on crop
965 development is suggested as a parsimonious way to improve model robustness in the future.

966

967 However, critical challenges remain to be addressed before the model can be used for such
968 prospective studies. In particular, more research is needed to better separate the effects of
969 rural land use change from other sources of variability and uncertainty in conceptual
970 catchment models [McIntyre et al., 2014]. Future work will focus on improving the estimation
971 of fractional snow-covered areas and the sensitivity of runoff generation components to
972 intense rainfall and protracted droughts. Results also highlight the need for a better
973 representation of surface water–groundwater interactions in the routing module. Given the
974 difficulty in estimating precipitation in the dry Andes, isotope-based studies could
975 considerably help to quantify the relative contributions of snowmelt, rainfall, ground water
976 and glacierized areas to streamflow [Ohlanders et al., 2013]. Such understanding is critical to
977 discriminate between several sources of errors and improve model reliability for use in impact
978 and adaptation studies.

979

980

981 **Appendix A**

982

983 Net shortwave and longwave radiations were computed as follows:

$$\Delta R_{SW} = (1 - \alpha)\tau R_e \quad (\text{A.I})$$

$$\Delta R_{LW} = \varepsilon_A \sigma (T_A + 273.15)^4 - \varepsilon_S \sigma (T_S + 273.15)^4 \quad (\text{A.II})$$

984 where α is the snow albedo, τ is the atmospheric transmissivity, R_e is the extraterrestrial
 985 radiation ($\text{MJ m}^{-2} \text{ day}^{-1}$) calculated from the latitude and the Julian day [Allen et al., 1998], σ
 986 is the Stefan-Boltzmann constant ($4.89 \cdot 10^{-15} \text{ MJ m}^{-2} \text{ K}^{-4}$), ε_S is the longwave emissivity for
 987 snow (0.97) and ε_A is the atmospheric longwave emissivity estimated as in Walter et al.
 988 [2005]. Snow albedo generally decreases between snowfalls as a result of metamorphic
 989 processes. This was represented in the model by adjusting an exponential decay rate related to
 990 the number of days since the last snowfall (N_t):

$$\alpha_t = \alpha_{\min} + (\alpha_{\max} - \alpha_{\min})e^{-k_a N_t} \quad (\text{A.III})$$

991 where α_{\min} and α_{\max} are the minimum and maximum snow albedos, and k_a is a recession
 992 factor. These parameters were determined from the literature [Lhermitte et al., 2014;
 993 Abermann et al., 2014] to prevent over-fitting (see Table 1). For shallow snowpacks such as
 994 those found around 30°S , albedo values also decrease during snowmelt periods as the
 995 influence of the underlying ground increases. This can have significant effects on melt rates,
 996 which were accounted for implicitly through the V_{\min} parameter in Eq. (5). Based on radiation
 997 data available over the last few years (not shown here), atmospheric transmissivity was set at
 998 0.75 under clear-sky conditions (precipitation $< 5 \text{ mm}$) and 0.4 on cloudy days (precipitation
 999 $\geq 5 \text{ mm}$).

1000

1001

1002 **Acknowledgements**

1003 The authors are very grateful to the *Centro de Estudios Avanzados en Zonas Áridas* (CEAZA)
 1004 for its essential logistic support during the field missions and to the *Dirección General de*
 1005 *Agua* (Chile) for providing the necessary meteorological and streamflow data. P. Hublart was
 1006 supported by a national PhD fellowship funded by the French Ministry of Higher Education
 1007 and Research. S. Lhermitte was supported as postdoctoral researcher for Fonds

1008 Wetenschappelijk Onderzoek–Vlaanderen. The Matlab program of the Snow Accumulation
1009 and Ablation model is available from the first author on request.

1010 **References**

- 1011 Abermann, J., Kinnard, C., and MacDonell, S.: Albedo variations and the impact of clouds on
1012 glaciers in the Chilean semi-arid Andes, *J. Glaciol.*, 60, 183–191, 2013.
- 1013 Adam, J. C., Hamlet, A. F., and Lettenmaier, D. P.: Implications of global climate change for
1014 snowmelt hydrology in the twenty-first century, *Hydrol. Process.*, 23, 962–972, 2009.
- 1015 Ajami, N. K., Hornberger, G. M., and Sunding, D. L.: Sustainable water resource
1016 management under hydrological uncertainty, *Water Resour. Res.*, 44, W11406,
1017 doi:10.1029/2007WR006736, 2008.
- 1018 Allen, R. G., Smith, M., Perrier, A., and Pereira, L. S.: Crop evapotranspiration – Guidelines
1019 for computing crop water requirements, Irrigation Drainage Paper 56, Food and Agric.
1020 Organ., Rome, Italy, 1998.
- 1021 Andréassian, V., Perrin, C., and Michel, C.: Impact of imperfect potential evapotranspiration
1022 knowledge on the efficiency and parameters of watershed models, *J. Hydrol.*, 286, 19–35,
1023 2004.
- 1024 Ashagrie, A. G., de Laat, P. J., de Wit, M. J., Tu, M. and Uhlenbrook, S.: Detecting the
1025 influence of land use changes on discharges and floods in the Meuse River Basin – the
1026 predictive power of a ninety-year rainfall-runoff relation?, *Hydrol. Earth Syst. Sci.*, 10,
1027 691–701, 2006.
- 1028 Ayala, A., McPhee, J., and Vargas, X.: Altitudinal gradients, midwinter melt, and wind effects
1029 on snow accumulation in semiarid midlatitude Andes under La Niña conditions, *Water*
1030 *Resour. Res.*, 50, 3589–3594, 2014.
- 1031 Ayala, A., Pellicciotti, F., MacDonell, S., McPhee, J., and Burlando, P.: Meteorological
1032 conditions associated to high sublimation amounts in semiarid high-elevation Andes
1033 decrease the performance of empirical melt models, EGU General Assembly 2015, 12–17
1034 April, 2015 in Vienna, Austria, 2015.
- 1035 Beven, K., Smith, P. J., and Wood, A.: On the colour and spin of epistemic error (and what
1036 we might do about it), *Hydrol. Earth Syst. Sci.*, 15, 3123–3133, 2011.
- 1037 Blöschl, G., and Montanari, A.: Climate change impacts – throwing the dice?, *Hydrol.*
1038 *Process.*, 24, 374–381, 2010.
- 1039 Boudhar, A., Hanich, L., Boulet, G., Duchemin, B., Berjamy, B., and Chehbouni, A.:
1040 Evaluation of the Snowmelt Runoff Model in the Moroccan High Atlas Mountains using
1041 two snow-cover estimates, *Hydrol. Sci. J.*, 54, 1094–1113, 2009.

1042 Bourgin, P.-Y ., Andréassian, V., Gascoïn, S., and Valéry, A. : Que sait-on des précipitations
1043 en altitude dans les Andes semi-arides du Chili ?, *Houille Blanche*, 2, 12–17, 2012.

1044 Brigode, P., Oudin, L., and Perrin, C.: Hydrological model parameter instability: A source of
1045 additional uncertainty in estimating the hydrological impacts of climate change?, *J.*
1046 *Hydrol.*, 476, 410–425, 2013.

1047 Brubaker, K., Rango, A., and Kustas, W.: Incorporating radiation inputs into the snowmelt
1048 runoff model, *Hydrol. Process.*, 10, 1329–1343, 1996.

1049 Caffarra, A., and Eccel, E.: Increasing the robustness of phenological models for *Vitis*
1050 *vinifera* cv. Chardonnay, *International Journal of Biometeorology*, 54, 255–267, 2010.

1051 Caffarra, A., and Eccel, E.: Projecting the impacts of climate change on the phenology of
1052 grapevine in a mountain area, *Aust. J. Grape Wine Res.*, 17, 52–61, 2011.

1053 Chuine, I.: A Unified Model for Budburst of Trees, *J. theor. Biol.*, 207, 337–347, 2000.

1054 Cleland, E. E., Chuine, I., Menzel, A., Harold, A. M., and Schwartz, M. D: Shifting plant
1055 phenology in response to global change, *Trends Ecol. Evol.*, 22, 357–365, 2007.

1056 Collet, L., Ruelland, D., Borrell-Estupina, V., Dezetter, A., and Servat, E.: Water supply
1057 sustainability and adaptation strategies under future anthropogenic and climatic changes
1058 of a meso-scale catchment, *Sci. Tot. Env.*, 536, 589–602, 2015.

1059 Duan, Q. Y., Gupta, V. K., and Sorooshian, S.: A shuffled complex evolution approach for
1060 effective and efficient global minimization, *J. Optim. Theory Appl.*, 76, 501–521, 1993.

1061 Duchêne, E., and Schneider, C.: Grapevine and climatic changes: a glance at the situation in
1062 Alsace, *Agron. Sustain. Dev.*, 25, 93–99, 2010a.

1063 Duchêne, E., Huard, F., Dumas, V., Schneider, C., and Merdinoglu, D.: The challenge of
1064 adapting grapevine varieties to climate change, *Clim. Res.*, 41, 193–204, 2010b.

1065 Engeland, K., Renard, B., Steinsland, I., and Kolberg, S.: Evaluation of statistical models for
1066 forecast errors from the HBV model, *J. Hydrol.*, 384, 142–155, 2010.

1067 Fabre, J., Ruelland, D., Dezetter, A., and Grouillet, B.: Accounting for hydro-climatic and
1068 water-use variability in the assessment of past and future water balance at the basin scale,
1069 In: *Hydrologic non-stationarity and extrapolating models to predict the future (Proc. of*
1070 *symp. HS02 held during IUGG2015 in Prague, Czech Republic, June 2015)*. IAHS Publ.,
1071 371, 43–48, 2015a.

1072 Fabre, J., Ruelland, D., Dezetter, A., and Grouillet, B.: Simulating past changes in the balance
1073 between water demand and availability and assessing their main drivers at the river basin
1074 scale, *Hydrol. Earth Syst. Sci.*, 19, 1263–1285, 2015b.

1075 Falvey, M., and Garreaud, R. D.: Wintertime precipitation episodes in central Chile:
1076 Associated meteorological conditions and orographic influences, *J. Hydrometeor.*, 8, 171–
1077 193, 2007.

1078 Favier, V., Falvey, M., Rabatel, A., Praderio, E., and López, D.: Interpreting discrepancies
1079 between discharge and precipitation in high-altitude area of Chile's Norte Chico region
1080 (26–32°S), *Water Resour. Res.*, 45, W02424, doi:10.1029/2008WR006802, 2009.

1081 Fenicia, F., Kavetski, D., and Savenije, H. H. G.: Elements of a flexible approach for
1082 conceptual hydrological modeling: 1. Motivation and theoretical development, *Water*
1083 *Resour. Res.*, 47, W11510, doi:10.1029/2010WR010174, 2011.

1084 Fila, G., Di Lena, B., Gardiman, M., Storchi, P., Tomasi, D., Silvestroni, O., and Pitacco, A.:
1085 Calibration and validation of grapevine budburst models using growth-room experiments
1086 as data source, *Agr. Forest. Meteorol.*, 160, 69–79, 2012.

1087 Fila, G., Gardiman, M., Belvini, P., Meggio, F., and Pitacco, A.: A comparison of different
1088 modelling solutions for studying grapevine phenology under present and future climate
1089 scenarios, *Agr. Forest. Meteorol.*, 195–196, 192–205, 2014.

1090 Fontaine, T. A., Cruickshank, T. S., Arnold, J. G., and Hotchkiss, R. H.: Development of a
1091 snowfall-snowmelt routine for mountainous terrain for the soil water assessment tool
1092 (SWAT), *J. Hydrol.*, 262, 209–223, 2002.

1093 García de Cortázar-Atauri, I., Daux, V., Garnier, E., Yiou, P., Viovy, N., Seguin, B.,
1094 Boursiquot, J. M., Parker, A. K., van Leeuwen, C., and Chuine, I.: Climate reconstructions
1095 from grape harvest dates: Methodology and uncertainties, *The Holocene* 20, 599–608,
1096 2010.

1097 Gascoïn, S., Lhermitte, S., Kinnard, C., Bortels, K., and Liston, G. E.: Wind effects on snow
1098 cover in Pascua-Lama, Dry Andes of Chile, *Adv. Water Resour.*, 55, 25–39, 2013.

1099 Gelman, A. G., and Rubin, D. B.: Inference from iterative simulation using multiple
1100 sequences, *Stat. Sci.* 7, 457–472, 1992.

1101 Gharari, S., Hrachowitz, M., Fenicia, F., Gao, H., and Savenije, H. H. G.: Using expert
1102 knowledge to increase realism in environmental system models can dramatically reduce
1103 the need for calibration, *Hydrol. Earth Syst. Sci.*, 18, 4839 – 4859, 2014.

1104 Greer, D. H., and Weedon, M. M.: The impact of high temperatures on *Vitis vinifera* cv.
1105 Semillon grapevine performance and berry ripening, *Front. Plant Sci.*, 4, 491, 2013.

1106 Gupta, H. V., Kling, H., Yilmaz, K. K., and Martinez, G. F.: Decomposition of the mean
1107 squared error and NSE performance criteria: Implications for improving hydrological
1108 modelling, *J. Hydrol.*, 377, 80–91, 2009.

1109 Harshburger, B. J., Humes, K. S., Walden, V. P., Moore, B. C., Blandford, T. R., and Rango,
1110 A.: Evaluation of Short-to-Medium Range Streamflow Forecasts Obtained Using an
1111 Enhanced Version of SRM, *J. Am. Water Resour. Assoc.*, 46, 603–617, 2010.

1112 Hendrickson, L., Ball, M. C., Wood, J. T., Chow, W. S., and Furbank, R. T.: Low temperature
1113 effects on photosynthesis and growth of grapevine, *Plant Cell Environ.*, 27, 795–809,
1114 2004.

1115 Hock, R.: Temperature index melt modelling in mountain areas, *J. Hydrol.*, 282, 104–115,
1116 2003.

1117 Hublart, P., Ruelland, D., Dezetter, A., and Jourde, H.: Reducing structural uncertainty in
1118 conceptual hydrological modeling in the semi-arid Andes, *Hydrol. Earth Syst. Sci.*, 19,
1119 2295–2314, 2015a.

1120 Hublart, P., Ruelland, D., García De Cortázar Atauri, I., and Ibacache, A.: Reliability of a
1121 conceptual hydrological model in a semi-arid Andean catchment facing water-use
1122 changes, *Proc. IAHS*, 371, 203–209, 2015b.

1123 Hughes, D. A., and Mantel, S. K.: Estimating the uncertainty in simulating the impacts of
1124 small farm dams on streamflow regimes in South Africa, *Hydrol. Sci. J.*, 55, 578–592,
1125 2010.

1126 Ibacache, A.: Cómo influye la temperatura sobre la época de cosecha en vides, *Tierra
1127 Adentro*, 81, 8–10, 2008.

1128 Ibacache, A., Martínez, L., Sturla, C., and Montes, C.: Zonificación del territorio de la
1129 denominación de origen Pisco, *Nuestro Pisco*, Programa de Innovación Territorial,
1130 Informe Final, 2010.

1131 Jin, X., Xu, C.-Y., Zhang, Q., and Singh, V. P.: Parameter and modeling uncertainty
1132 simulated by GLUE and a formal Bayesian method for a conceptual hydrological model,
1133 *J. Hydrol.*, 383, 147–155, 2010.

1134 Jones, G. V., White, M. A., Cooper, O. R., and Storchmann, K.: Climate change and global
1135 wine quality, *Climatic Change*, 73, 319–343, 2005.

1136 Kalthoff, N., Fiebig-Wittmaack, M., Meißner, C., Kohler, M., Uriarte, M., Bischoff-Gauß, I.,
1137 and Gonzales, E.: The energy balance, evapo-transpiration and nocturnal dew deposition
1138 of an arid valley in the Andes, *J. Arid Environ.*, 65, 420–443, 2006.

1139 Kim, H. S., Croke, B. F. W., Jakeman, A. J., Chiew, F., and Mueller, N.: Towards separation
1140 of climate and land use effects on hydrology: data analysis of the Googong and Cotter
1141 Catchments, In: Oxley, L., Kulasiri, D. (Eds.), *MODSIM 2007 International Congress on*

1142 Modelling and Simulation, Modelling and Simulation Society of Australia and New
1143 Zealand, 74–80, 2007.

1144 Kiptala, J. K., Mul, M. L., Mohamed, Y. A., and van der Zaag, P.: Modelling stream flow and
1145 quantifying blue water using a modified STREAM model for a heterogeneous, highly
1146 utilized and data-scarce river basin in Africa, *Hydrol. Earth Syst. Sci.* 18, 2287–2303,
1147 2014.

1148 Koskela, J. J., Croke, B. W. F., Koivusalo, H., Jakeman, A. J., and Kokkonen, T.: Bayesian
1149 inference of uncertainties in precipitation-streamflow modeling in a snow affected
1150 catchment, *Water Resour. Res.*, 48, W11513, doi:10.1029/2011WR011773, 2012.

1151 Laio, F., and Tamea, S.: Verification tools for probabilistic forecasts of continuous
1152 hydrological variables, *Hydrol. Earth Syst. Sci.*, 11, 1267–1277, 2007.

1153 Le Moine, N., Andréassian, V., Perrin, C., and Michel, C.: How can rainfall-runoff models
1154 handle intercatchment groundwater flows? Theoretical study based on 1040 French
1155 catchments, *Water Resour. Res.* 43, W06428, doi:10.1029/2006WR005608, 2007.

1156 Lhermitte, S., Abermann, J., and Kinnard, C.: Albedo over rough snow and ice surfaces,
1157 *Cryosphere* 8, 1069–1086, 2014.

1158 L'hôte, Y., Chevallier, P., Coudrain, A., Lejeune, Y., and Etchevers, P.: Relationship between
1159 precipitation phase and air temperature: comparison between the Bolivian Andes and the
1160 Swiss Alps, *Hydrol. Sci. J.*, 50, 989–997, 2005.

1161 MacDonell, S., Kinnard, C., Mölg, T., Nicholson, L., and Abermann, J.: Meteorological
1162 drivers of ablation processes on a cold glacier in the semiarid Andes of Chile, *The*
1163 *Cryosphere*, 7, 1833–1870, 2013.

1164 McIntyre, N., Ballard, C., Bruen, M., Bulygina, N., Buytaert, W., Cluckie, I., Dunn, S., Ehret,
1165 U., Ewen, J., Gelfan, A., Hess, T., Hughes, D., Jackson, B., Kjeldsen, T. R., Merz, R.,
1166 Park, J.-S., O'Connell, E., O'Donnell, G., Oudin, L., Todini, E., Wagener, T., and
1167 Wheeler, H.: Modelling the hydrological impacts of rural land use change, *Hydrol. Res.*,
1168 45, 737–754, 2014.

1169 Merritt, W. S., Croke, B. F. W., Jakeman, A. J., Letcher, R. A., and Perez, P.: A biophysical
1170 toolbox for assessment and management of land and water resources in rural catchments
1171 in northern Thailand, *Ecol. Model.*, 171, 279–300, 2004.

1172 Montanari, A.: Interactive comment on “ On the colour and spin of epistemic error (and what
1173 we might do about it)”, *Hydrol. Earth Syst. Sci.* 15, 3123–3133, 2011.

1174 Montecinos, A., and Aceituno, P.: Seasonality of the ENSO-Related Rainfall Variability in
1175 Central Chile and Associated Circulation Anomalies, *J. Climate*, 16, 281–296, 2003.

1176 Nicolle, P., Pushpalatha, R., Perrin, C., Francois, D., Thiéry, D., Mathevet, T., Le Lay, M.,
1177 Besson, F., Soubeyroux, J. M., Viel, C., Regimbeau, F., Andréassian, V., Maugis, P.,
1178 Augeard, B., and Morice, E.: Benchmarking hydrological models for low-flow simulation
1179 and forecasting on French catchments, *Hydrol. Earth Syst. Sci.*, 18, 2829–2857, 2014.

1180 Ohlanders, N., Rodriguez, M., and McPhee, J.: Stable water isotope variation in a Central
1181 Andean watershed dominated by glacier and snowmelt, *Hydrol. Earth Syst. Sci.*, 17,
1182 1035–1050, 2013.

1183 Ohmura, A.: Physical Basis for the Temperature-Based Melt-Index Method, *J. Appl.*
1184 *Meteor.*, 40, 753–761, 2001.

1185 Oudin, L., Hervieu, F., Michel, C., Perrin, C., Andreassian, V., Anctil, F., and Loumagne, C.:
1186 Which potential evapotranspiration input for a lumped rainfall-runoff model? Part 2:
1187 towards a simple and efficient potential evapotranspiration model for rainfall-runoff
1188 modelling, *J. Hydrol.*, 303, 290–306, 2005.

1189 Oudin, L., Perrin, C., Mathevet, T., Andréassian, V., and Michel, C.: Impact of biased and
1190 randomly corrupted inputs on the efficiency and the parameters of watershed models, *J.*
1191 *Hydrol.*, 320, 62–83, 2006.

1192 Palliotti, A., Tombesi, S., Silvestroni, O., Lanari, V., Gatti, M., and Poni, S.: Changes in
1193 vineyard establishment and canopy management urged by earlier climate-related grape
1194 ripening: A review, *Sci. Hort.*, 178, 43–54, 2014.

1195 Parker, A., Garcia de Cortázar-Atauri, I., Chuine, I., Barbeau, G., Bois, B., Boursiquot, J. M.,
1196 Cahurel, J. Y., Claverie, M., Dufourcq, T., Gény, L., Guimberteau, G., Hofmann, R. W.,
1197 Jacquet, O., Lacombe, T., Monamy, C., Ojeda, H., Panigai, L., Payan, J. C., Lovelle, B.
1198 R., Rouchaud, E., Schneider, C., Spring, J. L., Storchi, P., Tomasi, D., Trambouze, W.,
1199 Trought, M., and van Leeuwen, C.: Classification of varieties for their timing of flowering
1200 and veraison using a modelling approach: A case study for the grapevine species *Vitis*
1201 *vinifera* L., *Agric. For. Meteorol.*, 180, 249–264, 2013.

1202 Pellicciotti, F., Helbing, J., Rivera, A., Favier, V., Corripio, J., Araos, J., Sicart, J. E., and
1203 Careno, M.: A study of the energy balance and melt regime on Juncal Norte Glacier,
1204 semi-arid Andes of central Chile, using melt models of different complexity, *Hydrol.*
1205 *Process.*, 22, 3980–3997, 2008.

1206 Perrin, C., Michel, C. and Andréassian, V.: Improvement of a parsimonious model for
1207 streamflow simulation, *J. Hydrol.*, 279, 275–289, 2003.

1208 Pushpalatha, R., Perrin, C., Le Moine, N., and Andréassian, V.: A downward structural
1209 sensitivity analysis of hydrological models to improve low-flow simulation, *J. Hydrol.*,
1210 411, 66–76, 2011.

1211 Pushpalatha, R., Perrin, C., Le Moine, N., Mathevet, T., and Andréassian, V.: A review of
1212 efficiency criteria suitable for evaluating low-flow simulations, *J. Hydrol.*, 420–421, 171–
1213 182, 2012.

1214 Ruelland, D., Dezetter, A., and Hublart, P.: Sensitivity analysis of hydrological modelling to
1215 climate forcing in a semi-arid mountainous catchment, In: *Hydrology in a changing world:
1216 environmental and human dimensions (Proc. 7th FRIEND-Water Int. Conf., Montpellier,
1217 France, 7–10 Oct. 2014)*, IAHS Publ., 363, 145–150, 2014.

1218 Salinas, C. X., Gironás, J., and Pinto, M.: Water security as a challenge for the sustainability
1219 of La Serena-Coquimbo conurbation in northern Chile: global perspectives and
1220 adaptation, *Mitig. Adapt. Strateg. Glob. Change*, DOI 10.1007/s11027-015-9650-3, 2015.

1221 Savenije, H. H. G.: HESS Opinions "Topography driven conceptual modelling (FLEX-
1222 Topo)", *Hydrol. Earth Syst. Sci.*, 14, 2681–2692, 2010.

1223 Scanlon, B. R., Keese, K. E., Flint, A. L., Flint, L. E., Gaye, C. B., Edmunds, M. W., and
1224 Simmers, I.: Global synthesis of groundwater recharge in semiarid and arid regions,
1225 *Hydrol. Process.*, 20, 3335–3370, 2006.

1226 Schaeffli, B., and Huss, M.: Integrating point glacier mass balance observations into
1227 hydrologic model identification, *Hydrol. Earth Syst. Sci.*, 15, 1227–1241, 2011.

1228 Schoups, G., and Vrugt, J. A.: A formal likelihood function for parameter and predictive
1229 inference of hydrologic models with correlated, heteroscedastic, and non-Gaussian
1230 errors, *Water Resour. Res.*, 46, W10531, doi:10.1029/2009WR008933, 2010.

1231 Schulz, N., Boisier, J. P., and Aceituno, P.: Climate change along the arid coast of northern
1232 Chile, *Int. J. Climatol.*, 32, 1803–1814, 2011.

1233 Schulz, O., and de Jong, C.: Snowmelt and sublimation: field experiments and modelling in
1234 the High Atlas Mountains of Morocco, *Hydrol. Earth Syst. Sci.*, 8, 1076–1089, 2004.

1235 Seibert, J., and McDonnell, J. J.: Land-cover impacts on streamflow: a change-detection
1236 modelling approach that incorporates parameter uncertainty, *Hydrol. Sci. J.*, 55, 316–332,
1237 2010.

1238 Siebert, S., and Döll, P.: Quantifying blue and green virtual water contents in global crop
1239 production as well as potential production losses without irrigation, *J. Hydrol.*, 384, 198–
1240 217, 2010.

- 1241 Smith, T., Sharma, A., Marshall, L., Mehrotra, R., and Sisson, S.: Development of a formal
1242 likelihood function for improved Bayesian inference of ephemeral catchments, *Water*
1243 *Resour. Res.* 46, W12551, doi:10.1029/2010WR009514, 2010.
- 1244 Sproles, E., Nolin, A. W., Rittger, K., and Painter, T. H.: Climate change impacts on maritime
1245 mountain snowpack in the Oregon Cascades, *Hydrol. Earth Syst. Sci.*, 17, 2581–2597,
1246 2013.
- 1247 Squeo, F. A., Veit, H., Arancio, G., Gutiérrez, J. R., Arroyo, M. T. K., and Olivares, N.:
1248 Spatial heterogeneity of high mountain vegetation in the Andean desert zone of Chile (30°
1249 S), *Mt. Res. Dev.*, 13, 203–209, 1993.
- 1250 Staudinger, M., Stahl, K., Seibert, J., Clark, M. P., and Tallaksen, L. M.: Comparison of
1251 hydrological model structures based on recession and low flow simulations, *Hydrol. Earth*
1252 *Syst. Sci.*, 15, 3447–3459, 2011.
- 1253 Stehr, A., Debels, P., Arumi, J. L., Romero, F., and Alcayaga, H.: Combining the Soil and
1254 Water Assessment Tool (SWAT) and MODIS imagery to estimate monthly flows in a
1255 datascarc Chilean Andean basin, *Hydrol. Sci. J.*, 54, 1053–1067, 2009.
- 1256 Thyer, M., Renard, B., Kavetski, D., Kuczera, G., Franks, S. W., and Srikanthan, S.: Critical
1257 evaluation of parameter consistency and predictive uncertainty in hydrological modeling:
1258 A case study using Bayesian total error analysis, *Water Resour. Res.*, 45, W00B14,
1259 doi:10.1029/2008WR006825, 2009.
- 1260 Valéry, A., Andréassian, V., and Perrin, C.: Regionalization of precipitation and air
1261 temperature over high-altitude catchments – learning from outliers, *Hydrol. Sci. J.*, 55,
1262 928–940, 2010a.
- 1263 Valéry, A.: Modélisation précipitations – débit sous influence nivale Elaboration d’un module
1264 neige et évaluation sur 380 bassins versants, PhD Thesis, Irstea, Paris: AgroParisTech,
1265 2010b.
- 1266 Valéry, A., Andréassian, V., and Perrin, C.: As simple as possible but not simpler: What is
1267 useful in a temperature-based snow-accounting routine? Part 2 – Sensitivity analysis of
1268 the Cemaneige snow accounting routine on 380 catchments, *J. Hydrol.*, 517, 1176–1187,
1269 2014.
- 1270 Verbist, K., Robertson, A. W., Cornelis, W. M., and Gabriels, D.: Seasonal predictability of
1271 daily rainfall characteristics in central northern Chile for dry-land management, *J. Appl.*
1272 *Meteorol. Clim.*, 49, 1938–1955, 2010.
- 1273 Villagra, P., García de Cortázar, V., Ferreyra, R., Aspillaga, C., Zúñiga, C., Ortega-Farias, S.,
1274 and Sellés, G.: Estimation of water requirements and Kc values of ‘Thompson Seedless’

1275 table grapes grown in the overhead trellis system, using the Eddy covariance method,
1276 *Chil. J. Agr. Res.*, 74, 213–218, 2014.

1277 Vrugt, J. A., ter Braak, C. J. F., Diks, C. G. H., Higdon, D., Robinson, B. A., and Hyman, J.
1278 M.: Accelerating Markov chain Monte Carlo simulation by differential evolution with
1279 self-adaptive randomized subspace sampling, *Int. J. Nonlin. Sci. Num.*, 10, 271–288,
1280 2009.

1281 Walter, M. T., Brooks, E. S., McCool, D. K., King, L. G., Molnau, M., and Boll, J.: Process-
1282 based snowmelt modeling : does it require more input data than temperature-index
1283 modeling?, *J. Hydrol.*, 300, 65–75, 2005.

1284 Wagener, T., Boyle, D. P., Lees, M. J., Wheater, H. S., Gupta, H. V., and Sorooshian, S.: A
1285 framework for development and application of hydrological models, *Hydrol. Earth
1286 System Sci.*, 5, 13–26, 2001.

1287 Wang, E., and Engel, T.: Simulation of Phenological Development of Wheat Crops, *Agric.
1288 Syst.*, 58, 1–24, 1998.

1289 Wang, Q. J., Robertson, D. E., and Chiew, F. H. S.: A Bayesian joint probability modeling
1290 approach for seasonal forecasting of streamflows at multiple sites, *Water Resour. Res.*, 45,
1291 W05407, doi:10.1029/2008WR007355, 2009.

1292 Webb, L. B., Whetton, P. H., and Barlow, E. W. R.: Modelled impact of future climate
1293 change on the phenology of winegrapes in Australia, *Aust. J. Grape Wine Res.*, 13, 165–
1294 175, 2007.

1295 Yang, T., Xu, C. Y., Shao, Q. X., Chen, X., Lu, G. H., and Hao, Z. C.: Temporal and spatial
1296 patterns of low-flow changes in the Yellow River in the last half century, *Stoch. Environ.
1297 Res. Risk Assess.*, 24, 297–309, 2010.

1298

1301 **Table 1** Initial range or value of each model parameter. The third column provides explanations on the meaning
 1302 of the parameters and their units (in brackets). The fourth column indicates whether parameters are calibrated or
 1303 fixed beforehand. (*) For more details on the GL function, see Schoups and Vrugt [2010].
 1304

Parameter	Model	Meaning	Calibration	Initial range or value
Phenological models (calibrated against observed phenological dates)				
t_0	UniChill	Starting date for chilling rates accumulation (–)	No	15 th April
a	UniChill	Shape parameter of the chilling bell-curve (–)	Yes	0.1 – 2
b	UniChill	Optimal chilling temperature (°C)	Yes	0 – 20
c	UniChill	Shape parameter of the sigmoidal curve (–)	No	-0.25
d	UniChill	Shape parameter of the sigmoidal curve (°C)	No	15
C_{BB}	UniChill	Critical chilling requirement (–)	Yes	4 – 100
F_{BB}	UniChill	Critical state of forcing for budburst (–)	Yes	10 – 200
T_{min}	WE	Minimum temperature (°C)	No	0
T_{opt}	WE	Optimum temperature (°C)	Yes	0 – 40
T_{max}	WE	Maximum temperature (°C)	No	40
F_{FB}	WE	Critical state of forcing for full bloom (–)	Yes	1 – 300
F_{HV}	WE	Critical state of forcing for harvest (–)	Yes	1 – 300
Hydrological models (calibrated against observed streamflow data)				
θ_s	SAA	Snowpack cold-content factor (–)	Yes	0 – 1
MF	SAA	Restricted melt factor (mm day ⁻¹)	Yes	0 – 20
T_{thr}	SAA	Snowmelt temperature threshold (°C)	No	0
α_{min}	SAA	Minimum snow albedo (–)	No	0.4
α_{max}	SAA	Maximum snow albedo (–)	No	0.8
k_a	SAA	Time-scale parameter for the albedo (day ⁻¹)	No	0.25
$X1$	GR4J	Capacity of the soil-moisture accounting store (mm)	Yes	0 – 2000
$X2$	GR4J	Groundwater exchange coefficient (mm)	Yes	-10 – 10
$X3$	GR4J	Capacity of the routing store (mm)	Yes	0 – 500
$X4$	GR4J	Unit hydrograph time base (day)	Yes	0 – 10
$K_{C,BB}$	IWU	Crop coefficient at budburst (–)	No	0
$K_{C,FB}$	IWU	Crop coefficient at full bloom (–)	No	0.7
$K_{C,HV}$	IWU	Crop coefficient at harvest (–)	No	1.4
$K_{C,LF}$	IWU	Crop coefficient at the end of leaf fall (–)	No	0
N_{LF}	IWU	Length of the post-harvest period (day)	No	60 (Moscatel Rosada) 120 (Flame Seedless)
Generalized Likelihood function (inferred together with the hydrological parameters) (*)				
σ_0	GL	Heteroscedasticity intercept (mm day ⁻¹)	Yes	0 – 1
σ_1	GL	Heteroscedasticity slope (–)	Yes	0 – 1
Φ_1	GL	Autocorrelation coefficient (–)	Yes	0 – 0.8
β	GL	Kurtosis parameter (–)	Yes	-1 – 1
ε	GL	Skewness parameter (–)	No	1
μ_b	GL	Bias parameter (mm day ⁻¹)	No	0

1306 **Table 2** Goodness-of-fit (calibration) and predicting performance (validation) of the phenological models.
 1307 RMSE, Root Mean Square Error; NSE, Nash-Sutcliffe Efficiency; Bias, mean difference between the observed
 1308 and predicted dates.

1309

Model	Calibration (whole dataset)						Leave-one-out cross-validation					
	Flame Seedless			Moscatel Rosada			Flame Seedless			Moscatel Rosada		
	RMSE (days)	NSE (-)	Bias (days)	RSME (days)	NSE (-)	Bias (days)	RMSE (days)	NSE (-)	Bias (days)	RMSE (days)	NSE (-)	Bias (days)
BB	3.0	0.89	0.3	3.4	0.80	-0.29	5.4	0.64	0.4	6.8	0.18	0.6
FB	6.0	0.16	-0.6	6.1	0.46	0.5	7.0	-0.13	-0.1	7.2	0.24	0.13
HV	4.0	0.51	0.5	3.4	0.92	0.0	5.2	0.16	0.7	7.9	0.55	2.2

1310

1311 **Table 3** Calibrated parameter values of the phenological models

1312

Variety	Budburst				Full bloom		Harvest	
	a (°C ⁻¹)	b (°C)	C_{BB} (-)	F_{BB} (-)	T_{opt} (°C)	F_{FB} (-)	T_{opt} (°C)	F_{HV} (-)
Flame Seedless	0.11	11.5	27.4	21.2	22.0	55.5	30.2	28.9
Moscatel Rosada	0.57	11.3	10.8	41.8	20.2	49.9	32.9	31.3

1313

1314 **Table 4** Goodness-of-fit (calibration) and predicting performance (validation) of the hydrological models.

1315

Model	Calibration (1985–1995)				Validation (1985–1995)				Snow Errors (2000–2011)				
	F _{obj} (-)	KGE _{inv} (-)	NSE (-)	RMSE (m ³ s ⁻¹)	F _{obj} (-)	KGE _{inv} (-)	NSE (-)	RMSE (m ³ s ⁻¹)	EZ 1 (%)	EZ 2 (%)	EZ 3 (%)	EZ 4 (%)	EZ 5 (%)
A	0.13	0.77	0.94	1.66	0.27	0.53	0.88	2.66	2	15	16	12	17
B	0.16	0.74	0.93	1.76	0.33	0.43	0.90	2.41	2	16	16	10	11
C	0.07	0.90	0.95	1.55	0.13	0.80	0.90	2.36	2	16	16	10	11

1316

1317 **Table 5** Sublimation rates and contribution to snow ablation over the period 2000–2011.

1318

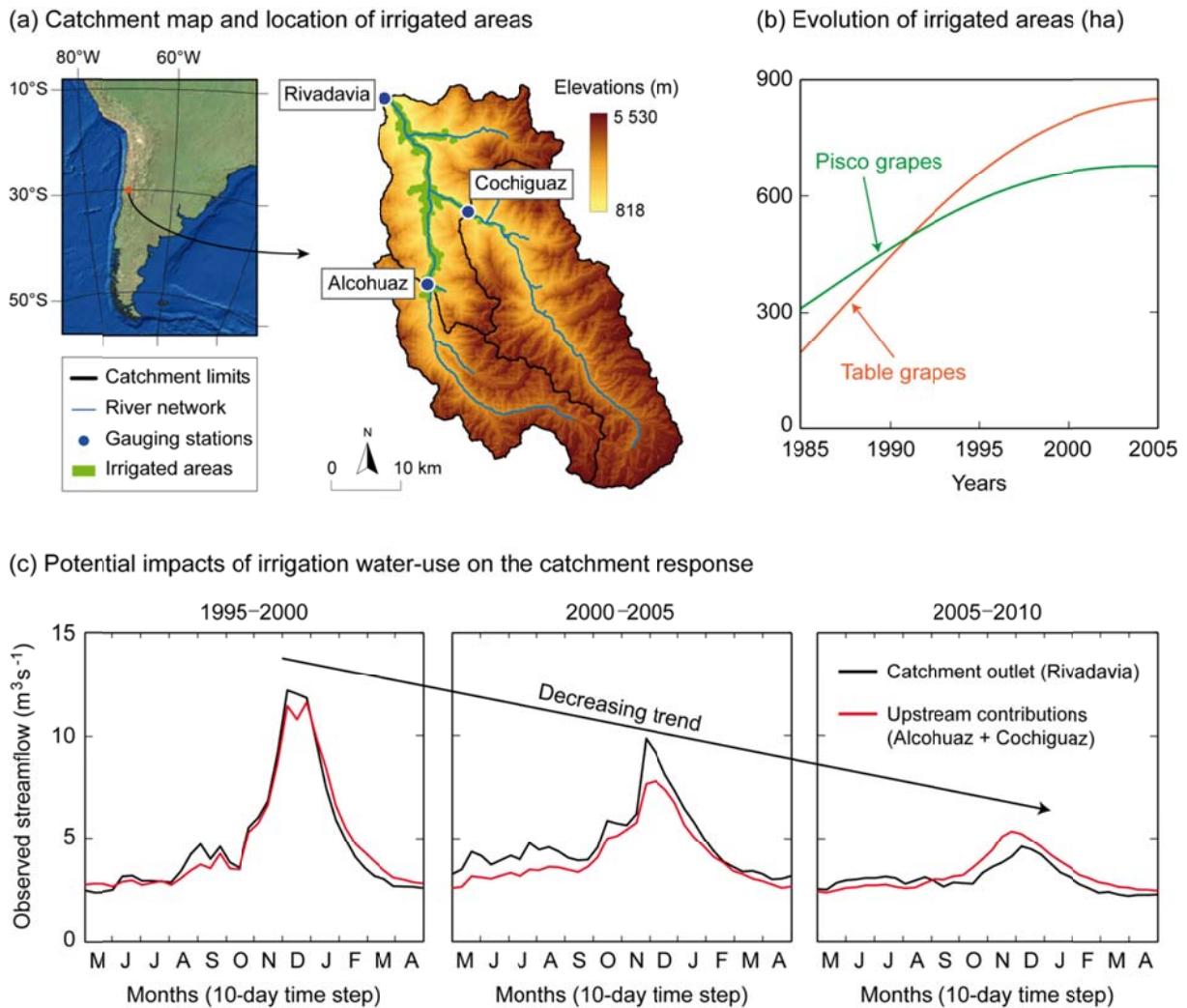
Model	Mean annual sublimation rates (mm day ⁻¹)					Sublimation / Ablation ratio (%)				
	EZ 1	EZ 2	EZ 3	EZ 4	EZ 5	EZ 1	EZ 2	EZ 3	EZ 4	EZ 5
B	0.00	0.07	0.30	0.75	1.11	0	4	11	26	36
C	0.00	0.07	0.31	0.75	1.11	0	4	12	26	37

1319

1320 **FIGURES & CAPTIONS**

1321

1322 **Figure 1** The Claro River catchment, Chile (30°S): (a) topography and current location of irrigated areas, (b)
 1323 evolution of irrigated areas since 1985 (interpolated from local cadastral surveys) for both types of grapes, and
 1324 (c) potential effects of increased irrigation water-use on mean annual hydrographs since the mid-1990s. These
 1325 effects were estimated from the difference between streamflow measured at the outlet in Rivadavia (in black)
 1326 and that measured at Cochiguaz and Alcohuaz (in red), which remains largely unaltered.
 1327



1328

1329

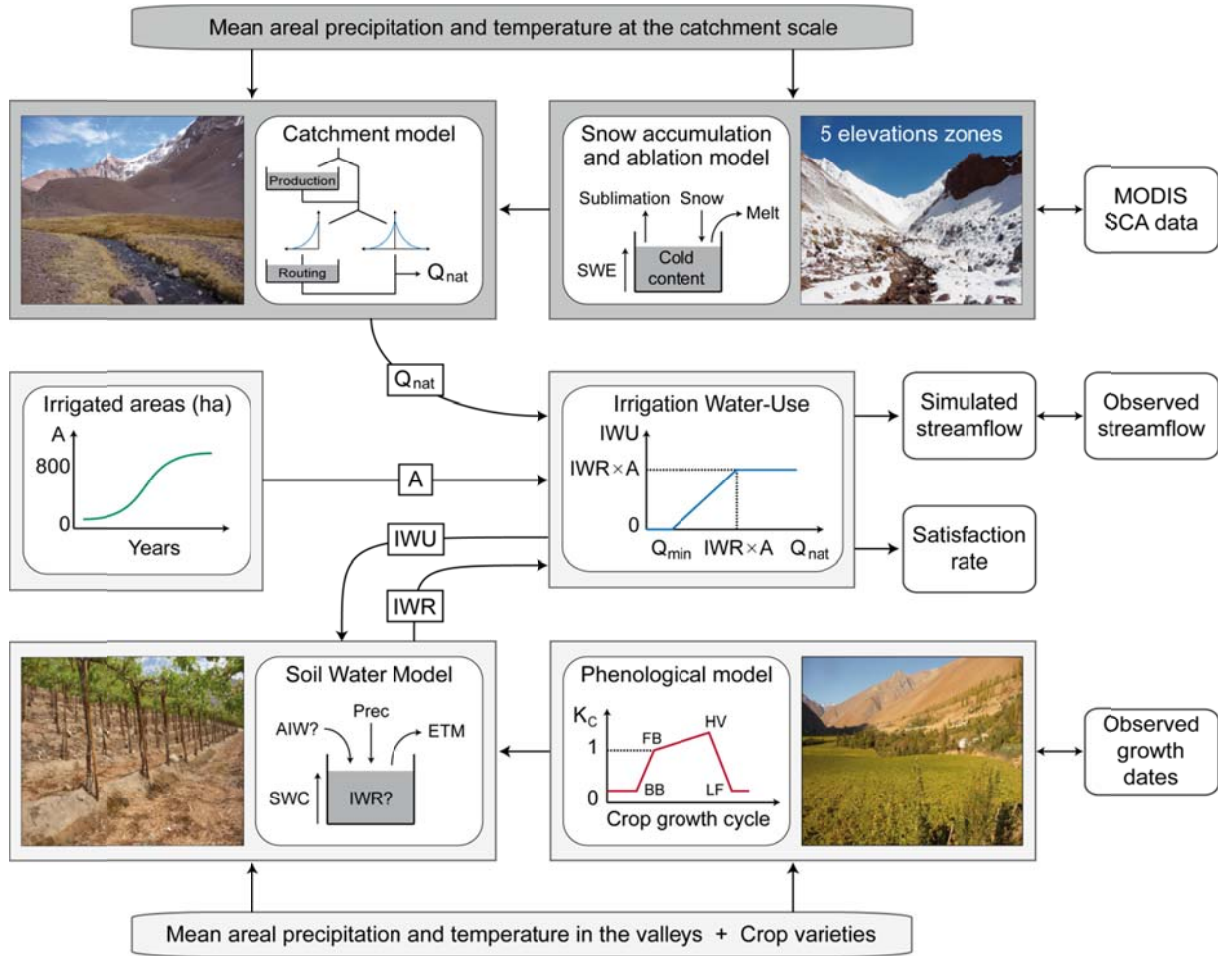
1330 **Figure 2** Block diagram of the lumped modeling framework developed in this study. The blue blocks refer to the hydrological part of the framework (used by Models A, B and C) while the green blocks relate to the estimation
 1331 of irrigation water requirements and irrigation water-use (used only by Model C). The simulated outputs and
 1332 observed data used for calibration/validation are indicated in orange. A satisfaction rate can also be computed
 1333 based on the ratio between water availability and irrigation requirements.
 1334

1335

1336

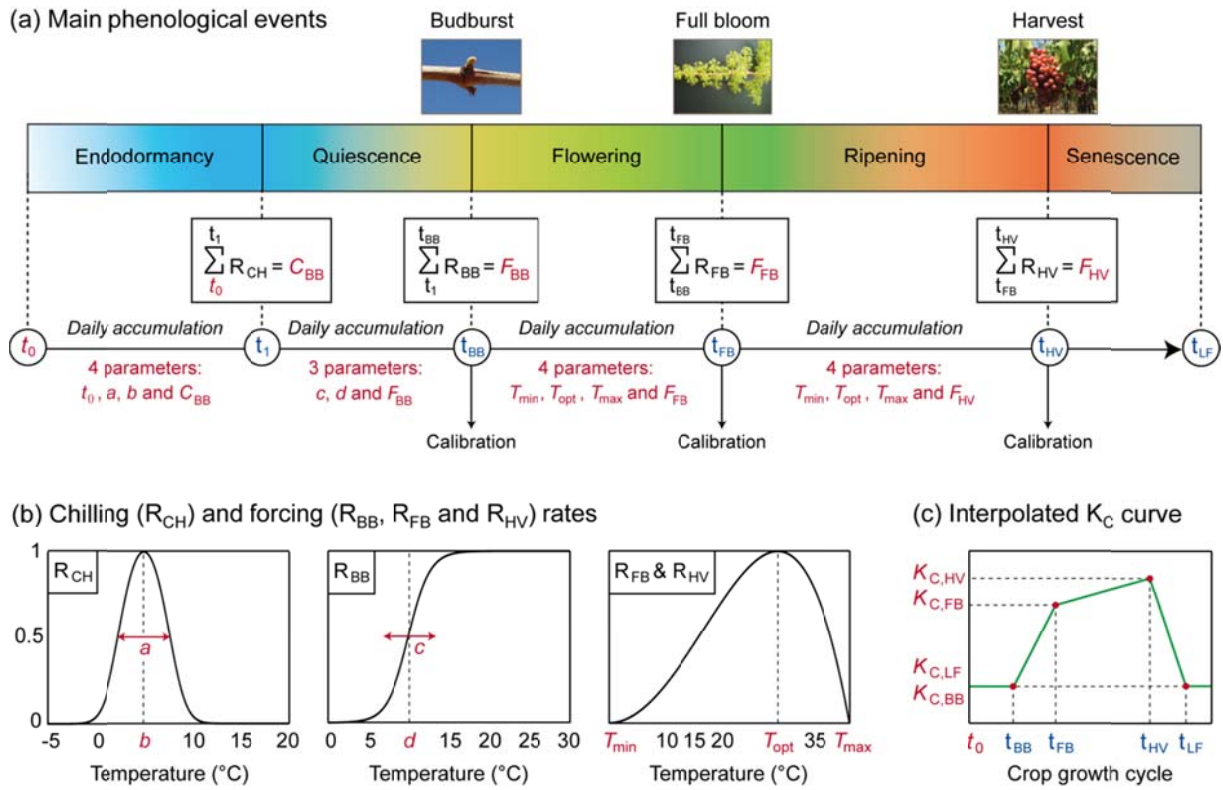
1337

1338



1339

1340 **Figure 3** Crop growth and water requirements modeling framework: (a) partitioning of the growing season into five phenophases and parameterization of each phenophase, (b) functions used to express the accumulated
 1341 chilling and forcing rates over each phenophase, and (c) translation of the simulated dates of budburst, full bloom and harvest into an interpolated K_C curve for use in the IWU model. Model parameters are indicated in
 1342 italic and colored in red. Note that parameters t_0 , c , d , T_{min} , T_{max} , $K_{C,BB}$, $K_{C,FB}$, $K_{C,HV}$ and $K_{C,LF}$ were fixed
 1343 beforehand to avoid over-parameterization.
 1344
 1345
 1346

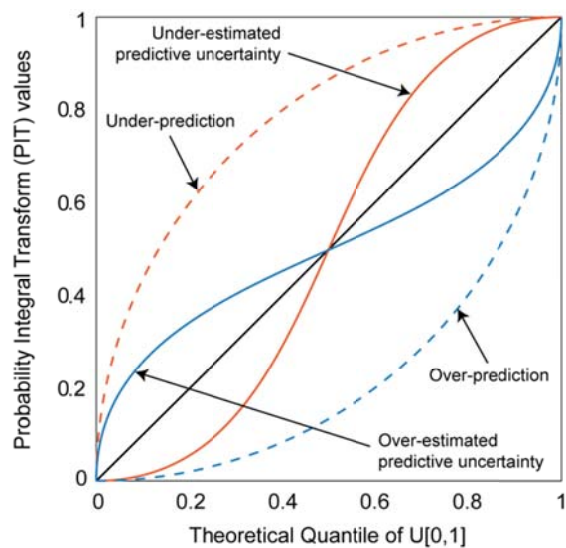


1349 **Figure 4** Possible interpretations of PIT plots (modified from Laio and Tamea [2007]). The diagonal line (in
1350 black) represents the ideal case.

1351

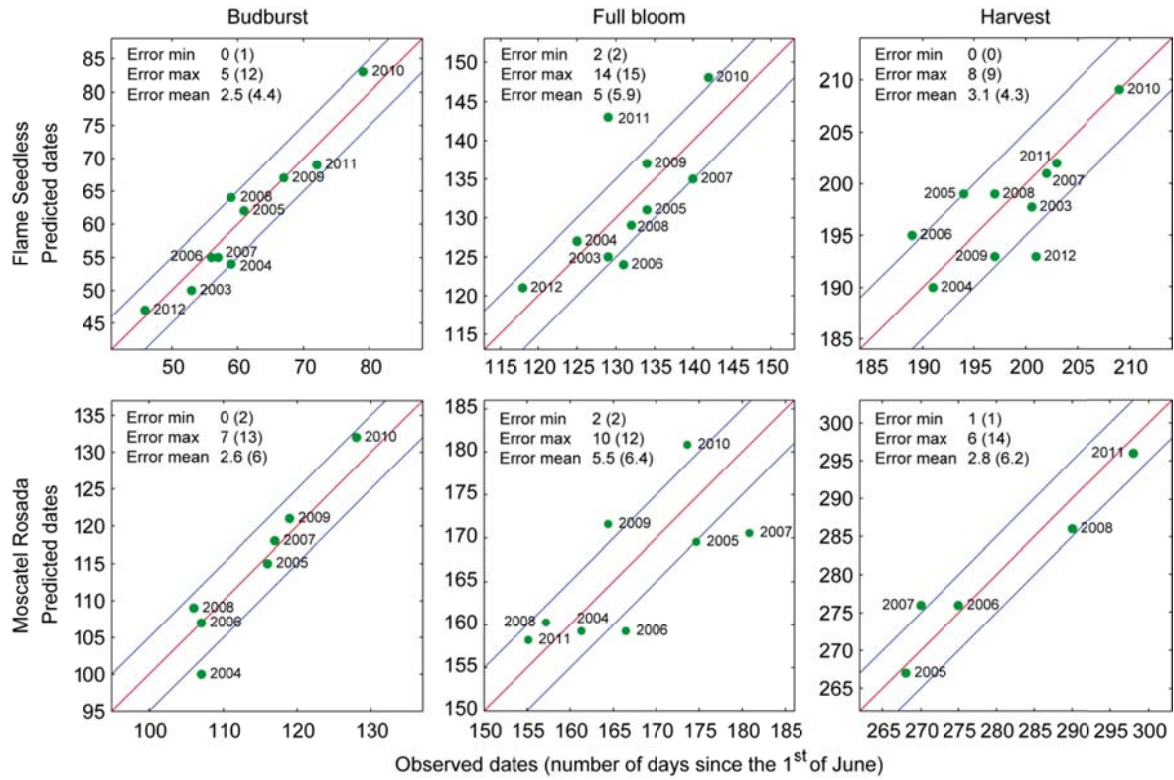
1352

1353



1354

1355 **Figure 5** Observed vs. predicted dates of budburst, full bloom and harvest for Flame Seedless and Moscatel
 1356 Rosada at the INIA experimental site. The dates are expressed in number of days since the 1st of June. The
 1357 minimum, maximum and mean absolute errors (in days) are given for each variety and stage of growth (the
 1358 values between brackets relate to the validation step while the values in front of the brackets relate to the
 1359 calibration step). The upper and lower blue lines indicate delays of ± 5 days between observed and predicted
 1360 dates, respectively.
 1361



1362

1363

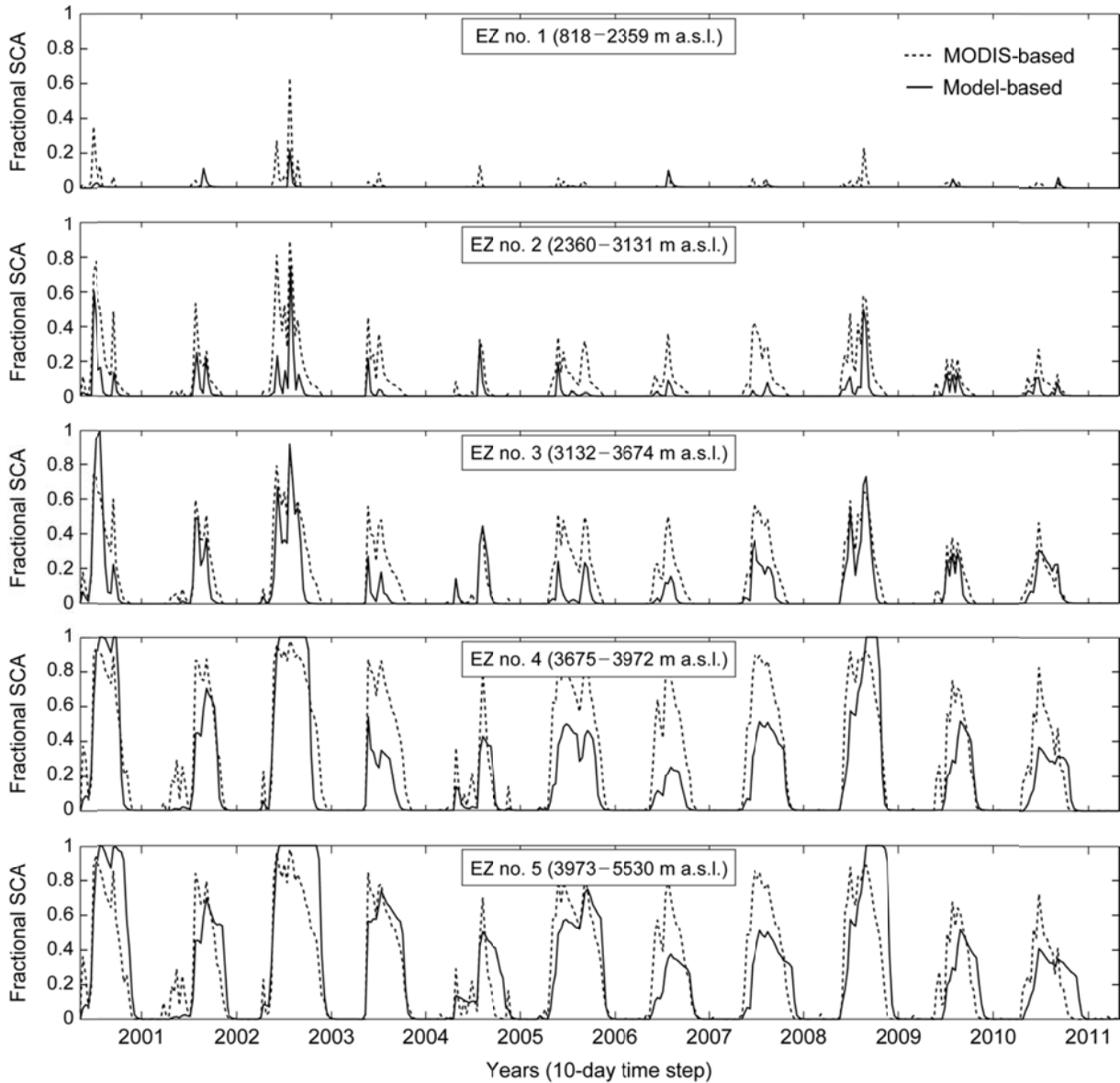
1364 **Figure 6** Comparison of simulated (i.e. Model C, accounting for sublimation) and observed (i.e. MODIS-based)
1365 fractional snow-covered areas (validation period). The graduations on the x -axis indicate the 1st of January of
1366 each year.

1367

1368

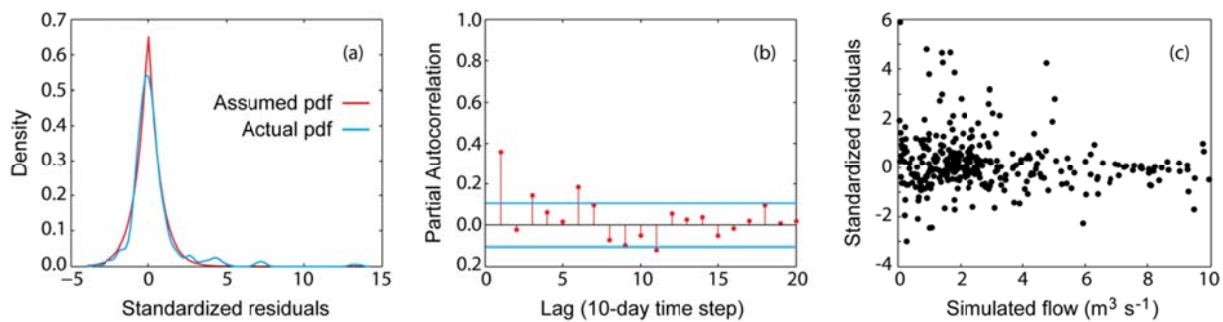
1369

1370



1371

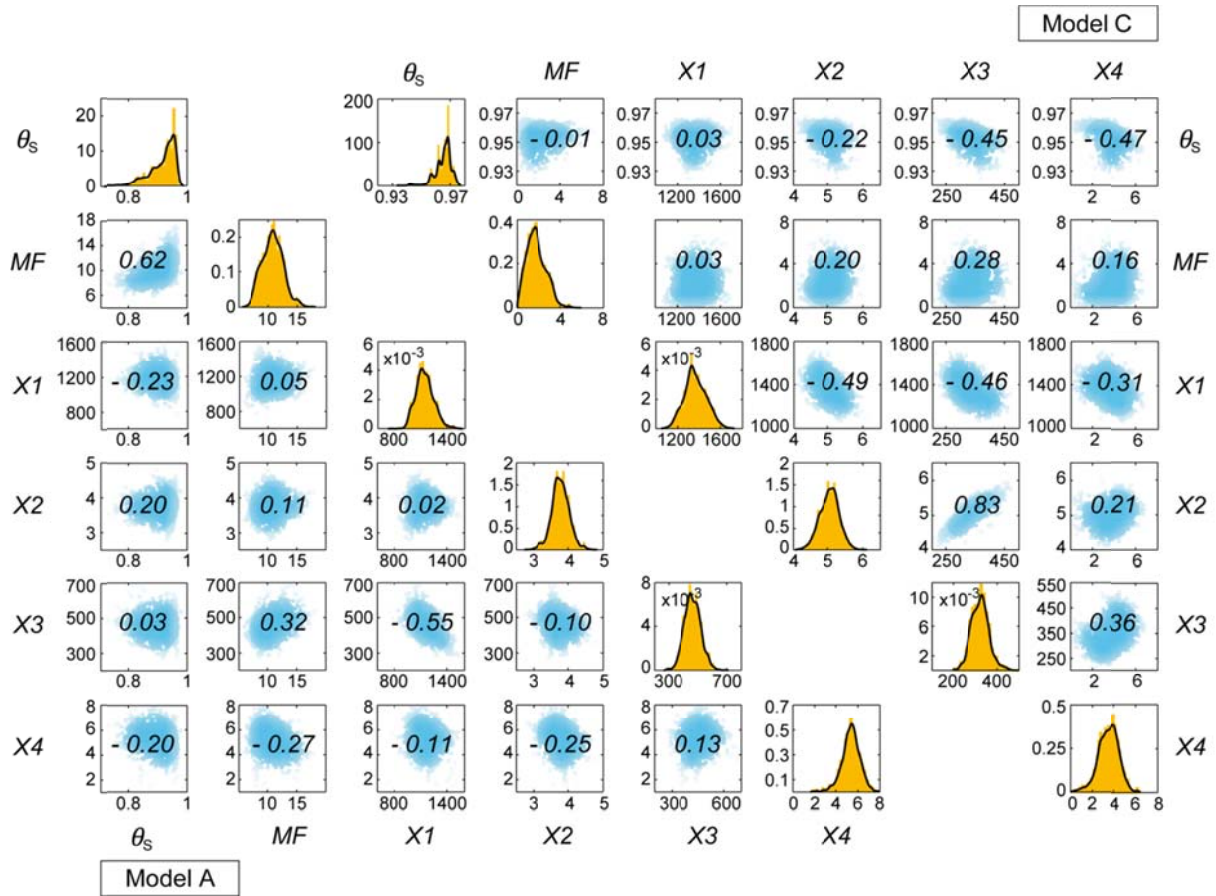
1372 **Figure 7** Formal checks of the statistical assumptions used to describe model residuals. Application to Model C
1373 (simulated for the validation period with the inferred maximum likelihood parameter set): (a) assumed and actual
1374 pdf; (b) partial autocorrelation; and (c) heteroscedasticity of standardized residuals.
1375



1376

1377

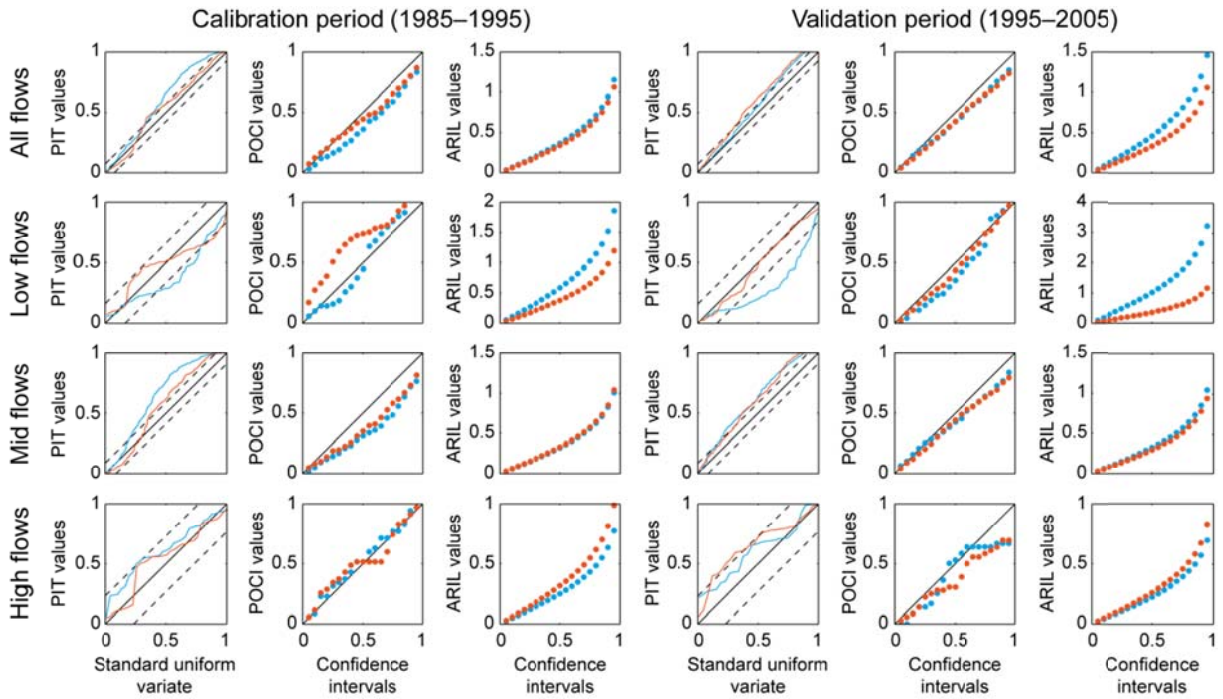
1378 **Figure 8** Two-dimensional scatter plots of the posterior parameter samples obtained with Models A and C. The
 1379 numbers in italic at the center of each cell indicate correlation coefficients. The histograms in orange represent
 1380 the marginal posterior distributions of parameters with superimposed kernel density estimates. The scatter plots
 1381 and histograms of Model B were not included here for brevity's sake, as they were very close to those of Model
 1382 C.
 1383



1384

1385

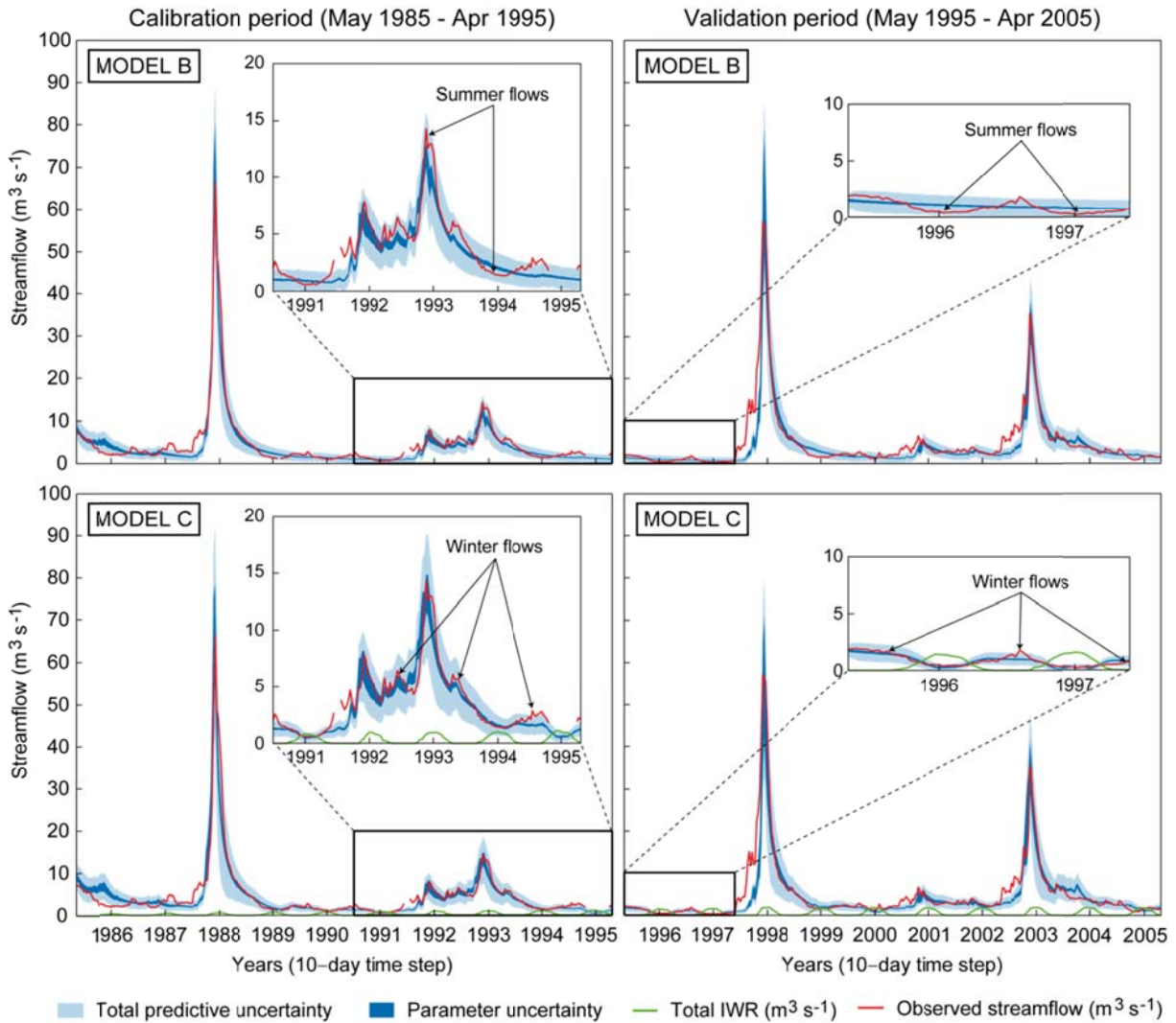
1386 **Figure 9** Posterior diagnostics used to evaluate the reliability (PIT, POCI) and resolution (ARIL) of the forecast
 1387 distributions obtained with Model B (in blue) and Model C (in red).
 1388



1389

1390

1391 **Figure 10** Predictive uncertainty bands obtained for both models with the DREAM algorithm and GL function.
 1392 The *dark blue* region represents the 95% confidence intervals associated with parameter uncertainty, whereas the
 1393 *light blue* region represents the 95% confidence intervals associated with parameter, model structure and input
 1394 errors. The graduations on the *x-axis* indicate the 1st of January of each year.
 1395



1396
 1397

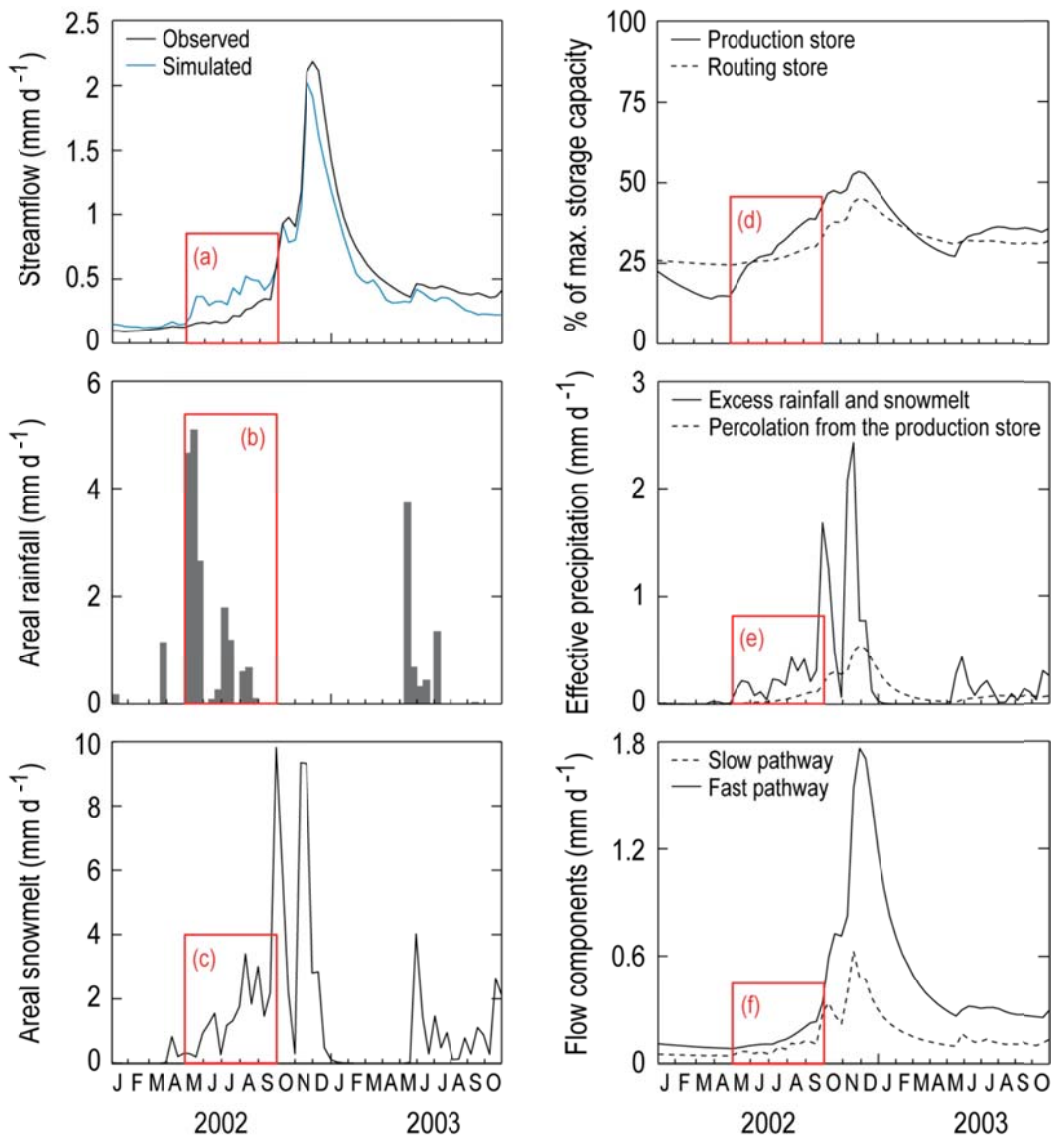
1398 **Figure 11** Internal state variables and fluxes obtained with Model C during the 2002–03 El Niño event (using
 1399 the best-performing parameter set obtained by calibration against the F_{obj} function).

1400

1401

1402

1403



1404

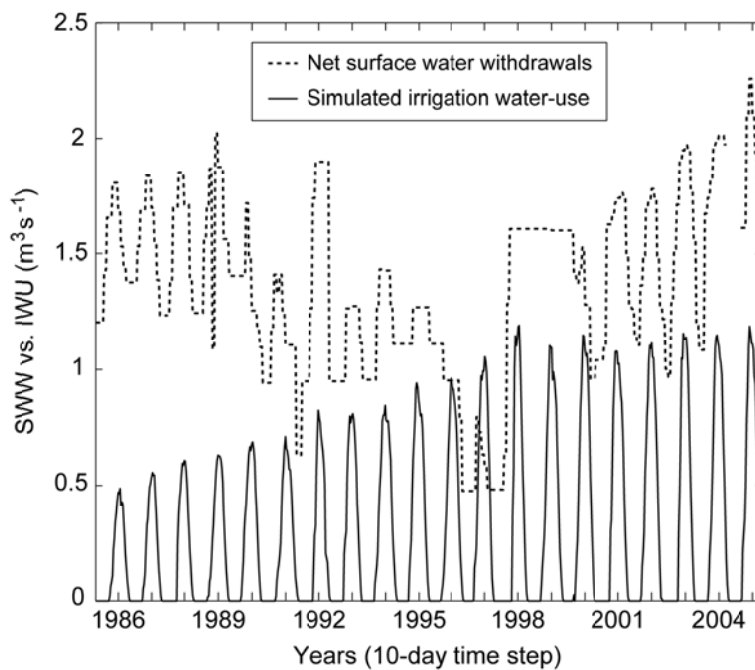
1405 **Figure 12** Comparison of net surface-water withdrawals (SWW) and irrigation water-use (IWU) at the
1406 catchment scale: SWW were obtained by considering monthly restrictions to water access entitlements provided
1407 by the Chilean authorities, a conveyance efficiency of 0.6 and a field application efficiency of 0.6 for pisco
1408 varieties and 0.9 for table varieties; IWU was obtained from model simulations.

1409

1410

1411

1412



1413